

Gross Moist Stability Assessment during TOGA COARE: Various Interpretations of Gross Moist Stability

KUNIAKI INOUE AND LARISSA E. BACK

University of Wisconsin–Madison, Madison, Wisconsin

(Manuscript received 23 March 2015, in final form 7 July 2015)

ABSTRACT

Daily averaged TOGA COARE data are analyzed to investigate the convective amplification/decay mechanisms. The gross moist stability (GMS), which represents moist static energy (MSE) export efficiency by large-scale circulations associated with the convection, is studied together with two quantities, called the critical GMS (a ratio of diabatic forcing to the convective intensity) and the drying efficiency [a version of the effective GMS (GMS minus critical GMS)]. The analyses reveal that convection intensifies (decays) via negative (positive) drying efficiency.

The authors illustrate that variability of the drying efficiency during the convective amplifying phase is predominantly explained by the vertical MSE advection (or vertical GMS), which imports MSE via bottom-heavy vertical velocity profiles (associated with negative vertical GMS) and eventually starts exporting MSE via top-heavy profiles (associated with positive vertical GMS). The variability of the drying efficiency during the decaying phase is, in contrast, explained by the horizontal MSE advection. The critical GMS, which is moistening efficiency due to the diabatic forcing, is broadly constant throughout the convective life cycle, indicating that the diabatic forcing always tends to destabilize the convective system in a constant manner.

The authors propose various ways of computing quasi-time-independent “characteristic GMS” and demonstrate that all of them are equivalent and can be interpreted as (i) the critical GMS, (ii) the GMS at the maximum precipitation, and (iii) a combination of feedback constants between the radiation, evaporation, and convection. Those interpretations indicate that each convective life cycle is a fluctuation of rapidly changing GMS around slowly changing characteristic GMS.

1. Introduction

Despite decades of advancement of conceptual theories and computational ability, it has still been challenging to correctly simulate tropical convective disturbances, such as convectively coupled equatorial waves (CCEWs) and the Madden–Julian oscillation (MJO), with realistic intensity and phase speed (e.g., Lin et al. 2006; Kim et al. 2009; Straub et al. 2010; Benedict et al. 2013). Current general circulation models used for climate predictions also fail to accurately simulate the position and strength of the intertropical convergence zone (ITCZ; e.g., Lin 2007). We know that one of the reasons for the difficulties is our lack of fundamental understanding of the interactions between deep convection and large-scale circulations in the tropics.

However, answering the question, “how, then, can we obtain better understanding of those interactions?” is a formidable task, because the problems to solve are generally too intricate to separate different causal contributions. To simplify the complex details in convective interactions, a conceptual quantity called the gross moist stability (GMS) has been investigated and has been proven to be useful in previous work. In this work, we utilize the GMS to look at mechanisms for convective amplification and decay in the Tropical Ocean and Global Atmosphere Coupled Ocean–Atmosphere Response Experiment (TOGA COARE) data.

The GMS, which represents efficiency of moist static energy export by large-scale circulations associated with moist convection, was originated by Neelin and Held (1987) with a simple two-layer atmospheric model. They described it as “a convenient way of summarizing our ignorance of the details of the convective and large scale transients.” Raymond et al. (2007) furthered this idea by defining the relevant quantity called the normalized gross moist stability (NGMS). Although different

Corresponding author address: Kuniaki Inoue, Department of Atmospheric and Oceanic Sciences, University of Wisconsin–Madison, 1225 W. Dayton St., Madison, WI 53706.
E-mail: inoue2@wisc.edu

authors have used slightly different definitions of the NGMS [see a review paper by Raymond et al. (2009)], all versions of the NGMS represent efficiency of export of some intensive quantity conserved in moist adiabatic processes per unit intensity of the convection. In this study, we utilize one version of the NGMS defined as

$$\Gamma \equiv \frac{\nabla \cdot \langle h\mathbf{v} \rangle}{\nabla \cdot \langle s\mathbf{v} \rangle} \quad (1)$$

where s is dry static energy (DSE), h is moist static energy (MSE), \mathbf{v} is horizontal wind, the del operator represents the isobaric gradient, and the angle brackets represent a mass-weighted vertical integral from the tropopause to the surface. In this study, we simply call Γ the GMS instead of the NGMS. We will show that this quantity and relevant ideas can be used to diagnose mechanisms for convective amplification and decay.

Previous GMS studies can be broadly categorized into two approaches: theoretical and diagnostic approaches. Although these two approaches are looking at the same quantity—namely, the GMS—it is usually difficult to compare their results to seek agreement between them. One of the difficulties arises from the simplification of vertical structures in the theoretical GMS studies.

Most of the theoretical GMS studies are inevitably dependent on an assumption of simple vertical structures. Historically, the GMS has been proven to be a powerful tool in the version of the quasi-equilibrium framework where temperature stratification is assumed to be close to a moist adiabat (e.g., Emanuel et al. 1994; Neelin and Zeng 2000). The perturbation vertical velocity then takes a first baroclinic mode structure, and the GMS is quasi time independent (or nearly constant). In this framework, the values of the GMS set the phase speed of features that have commonalities with CCEWs (e.g., Emanuel et al. 1994; Neelin and Yu 1994; Tian and Ramanathan 2003; Raymond et al. 2009).

Recent observational studies, however, show that the vertical structures of the CCEWs are not explained only by the first baroclinic mode but require the second baroclinic mode [e.g., Kiladis et al. (2009) and references therein]. Some theoretical studies have attempted to include the second baroclinic mode and succeeded in producing realistic structures of the CCEWs (e.g., Mapes 2000; Khouider and Majda 2006; Kuang 2008a,b). In such frameworks, however, the GMS is not attractive as a quantity that controls phase speed and linear instability of CCEWs, because the second baroclinic mode inevitably causes singularities of the GMS, making it blow up to infinity at some points (e.g., Inoue and Back 2015). Raymond and Fuchs (2007) and Fuchs et al. (2012) found in their simple models, which can also

produce variable vertical structures, that the dependency of the phase speed of equatorial gravity waves on the GMS is subtle.

The GMS also plays an important role in theoretical MJO studies. Recently, the idea emerged that the MJO is a moisture mode (Fuchs and Raymond 2007)¹, and some simple linear model studies demonstrated that the moisture mode becomes unstable when the GMS or “effective” GMS, including radiative or surface flux feedbacks, is negative (Fuchs and Raymond 2007; Raymond and Fuchs 2007; Raymond et al. 2009; Fuchs et al. 2012; and others).

The recent diagnostic GMS studies have focused more on the highly time-dependent property of the GMS (e.g., Hannah and Maloney 2011; Benedict et al. 2014; Hannah and Maloney 2014; Masunaga and L’Ecuyer 2014; Sobel et al. 2014; Inoue and Back 2015). Specifically, those studies have focused on the aspect of the GMS as a quantity that describes the destabilization/stabilization mechanisms of the convective disturbances. Episodes of organized convective disturbances generally begin with a bottom-heavy vertical velocity profile, which progressively evolves into a top-heavy profile as the convection develops. As in Fig. 1, a bottom-heavy profile with MSE-rich-lower-tropospheric convergence and MSE-poor-midtropospheric divergence leads to net import of MSE by the vertical circulation and thus destabilizes the convective system via column moistening; this condition is associated with negative GMS. Conversely, a top-heavy profile with MSE-poor midtropospheric convergence and MSE-rich upper-tropospheric divergence is associated with net export of MSE and positive GMS, which causes the convection to decay. These destabilization/stabilization mechanisms play crucial roles in the dynamics of the CCEWs in cloud-resolving model simulations (e.g., Peters and Bretherton 2006; Kuang 2008a).

In this study, we focus our attention on the diagnostic aspect of the GMS. We propose useful applications of the GMS to diagnoses of tropical convective disturbances. First, by utilizing the time dependency of the GMS, we claim that the destabilization/stabilization mechanisms discussed above play crucial roles in short-time-scale tropical disturbances and that those mechanisms can be extracted by investigating the GMS in observational data. Second, we propose some methods to calculate a meaningful value of the quasi-time-independent GMS for

¹ Other studies [Yu and Neelin (1994), and many others] also suggested modes that correspond to the “moisture mode” with different names. For a concise summary about the terminology, refer to the introduction in Sugiyama (2009).

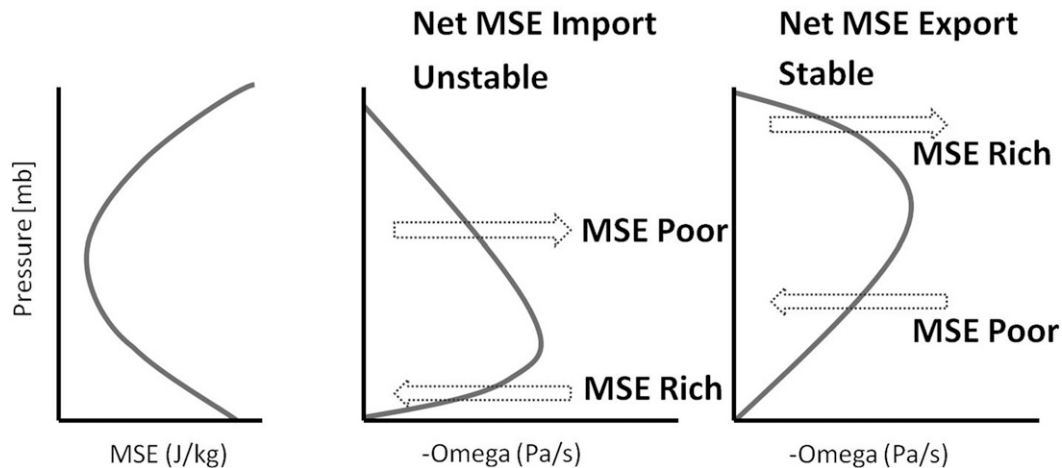


FIG. 1. Schematic figures of a typical MSE profile and vertical velocity (ω) profiles in a bottom-heavy and a top-heavy shape. The leftward (rightward) arrows correspond to convergence (divergence).

which computations and interpretations are relatively easy.

The rest of this paper is structured as follows. [Section 2](#) describes the dataset we used (the TOGA COARE dataset). [Section 3](#) sets forth the theoretical framework of the relationship between the time-dependent GMS and amplification/decay of convection. In this section, we introduce new quantities called the critical GMS (a ratio of diabatic forcing to the convective intensity) and drying efficiency [a version of the effective GMS (GMS minus critical GMS)]. By investigating those quantities in the TOGA COARE data, we demonstrate the amplification/decay mechanisms of the convection in [section 4](#). In [section 5](#), we extend our arguments toward the time-independent aspect of the GMS. In this section, we suggest some methods to calculate the quasi-time-independent GMS and clarify the interpretations of that. In [section 6](#), we summarize our arguments.

2. Data description

We investigate the field campaign data from TOGA COARE ([Webster and Lukas 1992](#)) to clarify the relationship between the GMS, vertical atmospheric structures (especially vertical velocity profiles), and convective amplification/decay. The TOGA COARE observational network was located in the western Pacific warm pool region. In this study, we analyze the data averaged over the spatial domain called the intensive flux array (IFA), which is centered at 2°S, 156°E, bounded by the polygon defined by the meteorological stations at Kapingamarangi and Kavieng and ships located near 2°S, 158°E and 4°S, 155°E. The sounding data were collected during the 4-month intensive observing period (IOP; 1 November

1992–28 February 1993) with 6-hourly time resolution. All variables are filtered with a 24-h running mean for a reason explained in the next section.

The dataset utilized was constructed by Minghua Zhang, who analyzed the sounding data by using an objective scheme called constrained variational analysis ([Zhang and Lin 1997](#)). In that scheme, the state variables of the atmosphere are adjusted by the smallest possible amount to conserve column-integrated mass, moisture, static energy, and momentum. See [Zhang and Lin \(1997\)](#) for more detailed information about the scheme.

3. Theoretical framework

Following [Yanai et al. \(1973\)](#), we start with the vertically integrated energy and moisture equations

$$\frac{\partial \langle s \rangle}{\partial t} + \langle \mathbf{v} \cdot \nabla s \rangle + \left\langle \omega \frac{\partial s}{\partial p} \right\rangle = \langle Q_R \rangle + LP + H \quad \text{and} \quad (2)$$

$$\frac{\partial \langle Lq \rangle}{\partial t} + \langle \mathbf{v} \cdot \nabla Lq \rangle + \left\langle \omega \frac{\partial Lq}{\partial p} \right\rangle = LE - LP, \quad (3)$$

where $s \equiv C_p T + gz$ is DSE; $C_p T$ is enthalpy; gz is geopotential; Q_R is radiative heating rate; L is the latent heat of vaporization, P is precipitation rate; H is surface sensible heat flux; q is specific humidity; E is surface evaporation; the angle brackets represent mass-weighted column integration from 1000 to 100 hPa; and the other terms have conventional meteorological meanings. Each quantity is averaged over the IFA. As in [Raymond et al. \(2009\)](#), assuming ω vanishes at the surface and tropopause pressures,

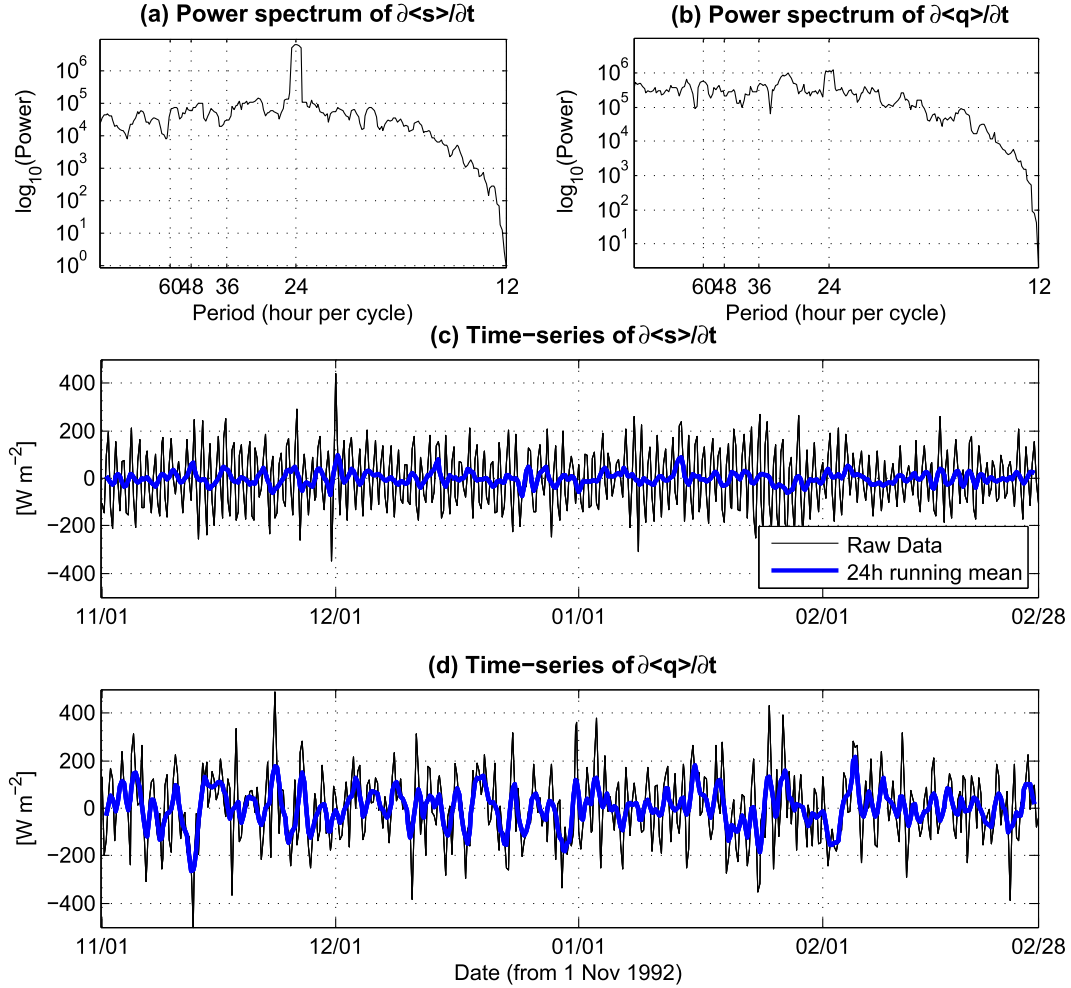


FIG. 2. (a) Power spectrum of $\partial\langle s \rangle / \partial t$. (b) Power spectrum of $\partial\langle q \rangle / \partial t$. (c) Time series of raw (black), and daily running-averaged $\partial\langle s \rangle / \partial t$ (blue) during TOGA COARE. (d) As in (c), but for $\partial\langle q \rangle / \partial t$. The specific humidity q is scaled into the energy unit by the latent heat of evaporation.

utilizing the continuity equation, and taking integration by parts yields

$$\frac{\partial\langle s \rangle}{\partial t} + \nabla \cdot \langle s \mathbf{v} \rangle = \langle Q_R \rangle + LP + H \quad \text{and} \quad (4)$$

$$\frac{\partial\langle Lq \rangle}{\partial t} + \nabla \cdot \langle Lq \mathbf{v} \rangle = LE - LP. \quad (5)$$

In the deep tropics, temperature anomalies are small because of weak rotational constraints (Charney 1963, 1969; Bretherton and Smolarkiewicz 1989), and thus the DSE tendency and horizontal DSE advective terms in Eqs. (2) and (4) are often assumed to be negligible, which is called the weak temperature gradient approximation (WTG; Sobel and Bretherton 2000; Sobel et al. 2001). When applying the WTG to observational data, however, we need to remove diurnal cycles of the temperature field, which is the primary exception to the

WTG. Figures 2a and 2b illustrate the power spectra of the column DSE and column moisture tendencies. These figures show that most variance of the column DSE tendency is explained by the diurnal cycle, while the diurnal cycle of the column moisture tendency is much smaller. Therefore, taking a daily running mean filter makes the column DSE tendency much less significant than the column moisture tendency, as illustrated in Figs. 2c and 2d, allowing us to neglect it. Neglecting the column DSE tendency and adding Eqs. (4) and (5) yields

$$\frac{\partial\langle Lq \rangle}{\partial t} \simeq -\nabla \cdot \langle h \mathbf{v} \rangle + \langle Q_R \rangle + S, \quad (6)$$

where $h \equiv s + Lq$ is MSE, and $S \equiv LE + H$ is surface fluxes. Generally, H is negligible over the tropical ocean.

We now utilize a relationship between precipitation and column-integrated water vapor $\langle q \rangle$ (i.e., precipitable

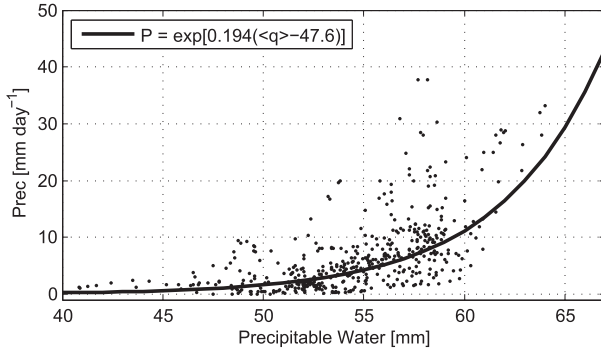


FIG. 3. Precipitation as a function of precipitable water $\langle q \rangle$. The black line was computed by a nonlinear least squares fitting.

water or water vapor path), which was shown by Bretherton et al. (2004). They showed the relation in the form of

$$P = \exp[a(\langle q \rangle - b)], \quad (7)$$

where a and b are some constants calculated by nonlinear least squares fitting. Figure 3 illustrates the relationship between the precipitation and precipitable water during TOGA COARE. The patterns statistically agree with the proposed exponential relationship. This exponential relationship is, however, not so crucial for this study. The ideas described below are valid as long as the precipitation has positive correlation with the precipitable water, which can be observed in the figure. Equation (7) can be replaced by a linearized form:

$$P = \frac{\langle q \rangle}{\tau_c}, \quad (8)$$

where τ_c is a convective adjustment time scale, as in the Betts–Miller parameterization (Betts 1986; Betts and Miller 1986), and the same conclusions can be drawn. Taking the natural logarithm of Eq. (7) and plugging it into Eq. (6) yields

$$\frac{L}{a} \frac{\partial \ln P}{\partial t} \simeq -\nabla \cdot \langle h\mathbf{v} \rangle + F, \quad (9)$$

where $F \equiv \langle Q_R \rangle + S$ is a diabatic source term.

Equation (9) indicates two convective phases:

$$\nabla \cdot \langle h\mathbf{v} \rangle - F < 0 \quad \text{and} \quad (10)$$

$$\nabla \cdot \langle h\mathbf{v} \rangle - F > 0. \quad (11)$$

According to Eq. (9), precipitation increases over time if a system is in the phase of Eq. (10), while it decreases in the phase of Eq. (11). Since the value of $\nabla \cdot \langle h\mathbf{v} \rangle - F$ is dependent on the intensity of the convection, it is advantageous to normalize it by the intensity of the

convection so that we can take composites of all the convective events with different intensities in the TOGA COARE data, and from that context, the concept of the GMS appears. A similar normalization technique has been utilized by Hannah and Maloney (2011).

In this study, we define a case with positive $\nabla \cdot \langle s\mathbf{v} \rangle$ to be convectively active and a case with negative $\nabla \cdot \langle s\mathbf{v} \rangle$ to be convectively inactive. Since we are interested in events when convection is happening, most of the analyses given below are conducted only for convectively active times. When convection is active, dividing Eqs. (10) and (11) by $\nabla \cdot \langle s\mathbf{v} \rangle$ yields

$$\Gamma - \Gamma_C < 0 \quad \text{and} \quad (12)$$

$$\Gamma - \Gamma_C > 0, \quad (13)$$

where

$$\Gamma_C = \frac{\langle Q_R \rangle + S}{\nabla \cdot \langle s\mathbf{v} \rangle}, \quad (14)$$

which we name the critical GMS. Here, Γ is the GMS defined in Eq. (1), and we call the quantity $\Gamma - \Gamma_C$ the drying efficiency. This drying efficiency can be viewed as a version of a quantity called the effective GMS (e.g., Su and Neelin 2002; Bretherton and Sobel 2002; Peters and Bretherton 2005; Sobel and Maloney 2012) and is similar to the effective GMS used in Hannah and Maloney (2014). We choose not to primarily refer to it as the effective GMS, because the effective GMS has generally described how convection responds to other MSE budget forcings (surface fluxes and/or horizontal advection), and, in the drying efficiency definition, all MSE budget terms have been folded in, so there is no longer a forcing term that the effective GMS is describing the response to. Nevertheless, if preferred, one can view the drying efficiency as a version of the effective GMS that includes horizontal MSE advection and surface fluxes in it.

When $\Gamma - \Gamma_C$ is negative (positive), the system is in the amplifying (decaying) phase in which convection intensifies (decays). (When convection is inactive with negative $\nabla \cdot \langle s\mathbf{v} \rangle$, those phases are reversed.) These hypotheses are not surprising, because $\Gamma - \Gamma_C$ is equivalent to

$$-\frac{1}{\nabla \cdot \langle s\mathbf{v} \rangle} \frac{\partial \langle Lq \rangle}{\partial t} \sim -\frac{1}{P} \frac{\partial \langle q \rangle}{\partial t}, \quad (15)$$

which represents efficiency of moisture discharge/recharge per unit intensity of convection, and the GMS and the critical GMS, respectively, represent contributions of MSE advection ($-\nabla \cdot \langle h\mathbf{v} \rangle$) and diabatic forcing ($F \equiv \langle Q_R \rangle + S$) terms to that efficiency. Therefore, the

phases of Eqs. (12) and (13) simply state that a moistened (dried) system leads to amplification (dissipation) of the convection. Despite the simplicity, this concept is useful from both diagnostic and theoretical perspectives.

We take composites of convective structures onto values of the drying efficiency. This composite method functions well because the drying efficiency is independent of the convective intensity (therefore, it is only a function of the convective structures) and is a good index of the convective stability.² Hence by using the drying efficiency composite method, we can illustrate the connection between convective structures and the stability of moist convection.

4. Results and discussion

a. Drying efficiency and convective amplification/decay

First, we need to verify the hypotheses of the amplifying and decaying phases, Eqs. (12) and (13), for convectively active times during TOGA COARE. When computing Γ and Γ_C , as suggested by Raymond et al. (2009), the time filter was applied to the numerator and denominator before taking the ratio between them. All data points with $\nabla \cdot \langle s\mathbf{v} \rangle$ less than 10 Wm^{-2} were removed to exclude convectively inactive times and to avoid division by zero. Furthermore, since we apply a binning average method to $\Gamma - \Gamma_C$, we excluded 2.5% outliers from the left and right tails of the PDF of $\Gamma - \Gamma_C$ before taking composites in order to avoid biases due to very large and small values.

Figure 4a shows precipitation changes as a function of the drying efficiency $\Gamma - \Gamma_C$. The precipitation changes were calculated by center differencing, and those were averaged in 12.5-percentile bins with respect to $\Gamma - \Gamma_C$. In the amplifying phase (negative $\Gamma - \Gamma_C$), the precipitation changes are positive, indicating the convection is enhanced; in the decaying phase (positive $\Gamma - \Gamma_C$), in contrast, the convection is attenuated. Figure 4b illustrates the probabilities of increase in precipitation as a function of the binned $\Gamma - \Gamma_C$. These probabilities were computed as a ratio of the number of the data points with positive precipitation changes to the total number of the data points within each 12.5-percentile bin of $\Gamma - \Gamma_C$. When $\Gamma - \Gamma_C$ is negative and large (-1.4 to -0.4) the probability of precipitation increase is greater than $\sim 70\%$, whereas, when $\Gamma - \Gamma_C$ is

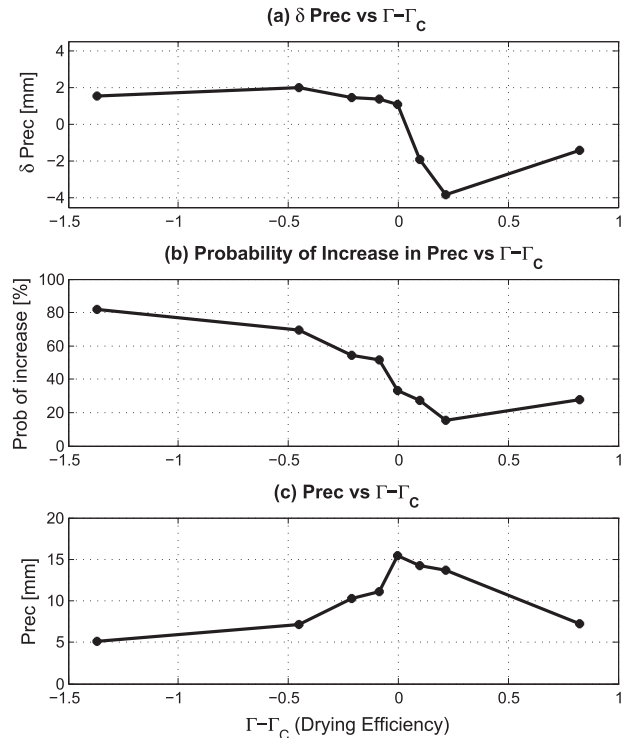


FIG. 4. (a) Binned precipitation changes as a function of the drying efficiency $\Gamma - \Gamma_C$, averaged in 12.5-percentile bins of $\Gamma - \Gamma_C$. The precipitation changes δP were computed by center differencing. (b) Binned probabilities of increase in precipitation as a function of $\Gamma - \Gamma_C$, averaged in the same bins as (a). The values subtracted from 100% represent probabilities of decrease in precipitation. (c) Binned precipitation as a function of $\Gamma - \Gamma_C$, computed in the same way as above. For this figure, all data points with $\nabla \cdot \langle s\mathbf{v} \rangle$ less than 10 Wm^{-2} were removed to exclude convectively inactive times and to avoid division by zero.

positive and large (0.2 to 0.8), the precipitation decreases at $\sim 80\%$. As $\Gamma - \Gamma_C$ increases from -0.4 to 0.2 , the probability of precipitation increase rapidly drops. Both Figs. 4a and 4b are consistent with the hypotheses of the amplification/decaying phases.

Figure 4c shows the precipitation as a function of the binned $\Gamma - \Gamma_C$. In the amplifying phase, the precipitation increases as $\Gamma - \Gamma_C$ becomes less negative and reaches the maximum when $\Gamma - \Gamma_C$ is zero, or Γ is equal to Γ_C ; in the decaying phase, the precipitation decreases with increase in $\Gamma - \Gamma_C$. This figure, together with Figs. 4a and 4b, indicates that values of the drying efficiency are statistically linked to convective development and dissipation; that is, convection generally begins with high efficiency of moistening (negative and large $\Gamma - \Gamma_C$), the efficiency of moistening gradually decreases (i.e., $\Gamma - \Gamma_C$ becomes less negative) as the convection develops, and, eventually, it starts to discharge moisture (positive $\Gamma - \Gamma_C$), leading to dissipation of the convection.

² In this study, we use the word “stability” to refer to the drying efficiency (or a version of the effective gross moist stability) and not to conventional thermodynamic stability, such as convective available potential energy (CAPE).

When interpreting Fig. 4 and the other drying efficiency figures given below, one caution is required; that is, those figures do not include any information about time. They were plotted in order of stability from the most unstable to the most stable, and not ordered in time, so the length of the x axis does not represent the actual duration of the corresponding structures. Nevertheless, because every phenomenon statistically evolves from unstable to stable conditions, those figures represent a statistical convective life cycle: the convection generally evolves from negative and large $\Gamma - \Gamma_C$ to positive and large $\Gamma - \Gamma_C$.

b. Variability of drying efficiency

In the last subsection, we verified that, when the drying efficiency $\Gamma - \Gamma_C$ is negative (positive), convection is enhanced (attenuated), respectively. Now let us investigate which processes cause variability of the drying efficiency, making the convection amplify or dissipate. In other words, we examine how moist convection evolves from unstable (negative $\Gamma - \Gamma_C$) into stable (positive $\Gamma - \Gamma_C$) conditions.

Variability of $\Gamma - \Gamma_C$ is separated into contributions of the GMS (or advective terms) and of the critical GMS (or diabatic forcing terms). Furthermore, GMS can be divided into horizontal and vertical components as

$$\Gamma = \Gamma_H + \Gamma_V, \quad (16)$$

where

$$\Gamma_H = \frac{\langle \mathbf{v} \cdot \nabla h \rangle}{\nabla \cdot \langle \mathbf{s} \mathbf{v} \rangle} \quad \text{and} \quad \Gamma_V = \frac{\left\langle \omega \frac{\partial h}{\partial p} \right\rangle}{\nabla \cdot \langle \mathbf{s} \mathbf{v} \rangle}.$$

Therefore, variability of the drying efficiency can be explained by three components: changes in the horizontal GMS Γ_H , in the vertical GMS Γ_V , and in the critical GMS Γ_C . Figure 5 shows those three components as a function of the binned $\Gamma - \Gamma_C$. By comparing the amount of the slope of each component with the slope of $\Gamma - \Gamma_C$, we can determine which processes explain the variability of the drying efficiency when it evolves from negative to positive values.

In this figure, Γ_C is broadly constant and maintains positive values around 0.25–0.5 along all the values of $\Gamma - \Gamma_C$. (Although it varies some, the variations are less significant compared to the other two components.) This indicates that Γ_C always decreases the value of $\Gamma - \Gamma_C$ toward negative values and thus forces the convective system toward the amplifying phase. The combination

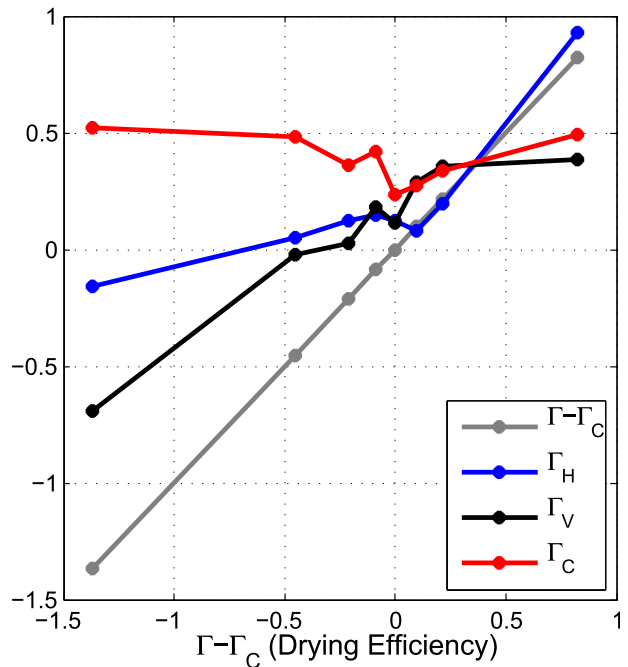


FIG. 5. Variability of each component, horizontal GMS Γ_H (blue), vertical GMS Γ_V (black), and critical GMS Γ_C (red), decomposed from drying efficiency $\Gamma - \Gamma_C$ (gray), and averaged in the same bins as in Fig. 4.

of radiative heating and surface fluxes, therefore, constantly creates a tendency toward destabilization as a moisture (or MSE) source, increasing efficiency of moistening (or decreasing the drying efficiency) during both the amplifying and decaying phases, and does not contribute to the variability of $\Gamma - \Gamma_C$. Therefore, given a constant value of Γ_C , convection intensifies (decays) when the GMS is less (greater) than that critical constant. More detailed discussions about Γ_C are provided in section 4d and section 5.

In the amplifying phase (i.e., $\Gamma - \Gamma_C < 0$), most of the slope of $\Gamma - \Gamma_C$ is explained by Γ_V . This indicates that vertical MSE advection mainly explains the convective evolution from the amplifying into the decaying phases. In this phase, Γ_H is broadly constant and nearly zero, implying the horizontal MSE (or moisture) advection does not contribute to amplification of the convection. When $\Gamma - \Gamma_C$ is ~ -1.4 , the values of Γ_H , Γ_V , and Γ_C are ~ -0.2 , ~ -0.7 , and ~ 0.5 , respectively. Hence, the system is primarily moistened by the vertical MSE advection, the radiative heating, and the surface fluxes. As the convection evolves toward the decaying phase, Γ_V becomes less negative, which indicates that moistening via vertical advection becomes less efficient. At $\Gamma - \Gamma_C \simeq -0.5$, Γ_H and Γ_V are nearly zero, while Γ_C is ~ 0.5 . In this stage, only the radiative heating and the surface fluxes moisten the convective system. As the convection

develops further to greater $\Gamma - \Gamma_C$, the vertical advection starts to discharge moisture (i.e., positive Γ_V), leading to dissipation of the convection. Therefore, what drives the convection from the amplifying into the decaying phase is the vertical MSE advection (associated with Γ_V), which at the beginning moistens the system, followed by discharge of moisture. During that evolution, Γ_C constantly tends to moisten the system, resisting the drying by the vertical advection.

In the decaying phase (i.e., $\Gamma - \Gamma_C > 0$), in contrast, the slope of Γ_H nicely matches the slope of $\Gamma - \Gamma_C$. Therefore, the drying efficiency in the fastest dissipation stage is mainly explained by the horizontal MSE advection. The vertical GMS Γ_V also keeps positive values in this phase, indicating the vertical advection also exports MSE and dries the system. But the horizontal advection dries the system more efficiently (i.e., $\Gamma_H > \Gamma_V$). The critical GMS Γ_C is relatively constant with positive values, making $\Gamma - \Gamma_C$ smaller. Therefore, in the decaying phase, both horizontal and vertical advection tend to dry the system, while the radiative heating and surface fluxes tend to supply MSE anomalies into the convective system.

c. Variability of vertical GMS

We have shown that, in the amplifying phase, most of the variability of the drying efficiency is explained by the vertical GMS Γ_V . Now we investigate how Γ_V varies. During TOGA COARE, 94% of the total variance of $\langle \omega \partial h / \partial p \rangle$ is explained by the variance of ω . Thus, the variability of Γ_V is mainly due to the fluctuations of ω profiles. The relationship between Γ_V and ω has been pointed out by previous studies (e.g., Back and Bretherton 2006; Peters and Bretherton 2006; Sobel and Neelin 2006; Sobel 2007; Raymond et al. 2009; Masunaga and L'Ecuyer 2014; Inoue and Back 2015). Those studies have demonstrated that bottom-heavy ω profiles that import MSE via lower-level convergence and middle-level divergence are associated with negative (or close to negative) values of Γ_V , while top-heavy profiles with middle-level convergence and upper-level divergence export MSE from the atmospheric column, causing positive and large Γ_V .

Figure 6a illustrates the relationship between Γ_V and ω profiles for convectively active times in the TOGA COARE data. The blue (red) shaded contours represent ascending (descending) motions. As described above, negative and large Γ_V is associated with bottom-heavy ω shapes, and as Γ_V increases ω becomes more top heavy. When the convection is inactive (i.e., $\nabla \cdot \langle s\mathbf{v} \rangle$ is negative; in Fig. 6b), the relation is reversed; that is, negative and large Γ_V corresponds to top-heavy ω with lower-tropospheric descending motion, while positive

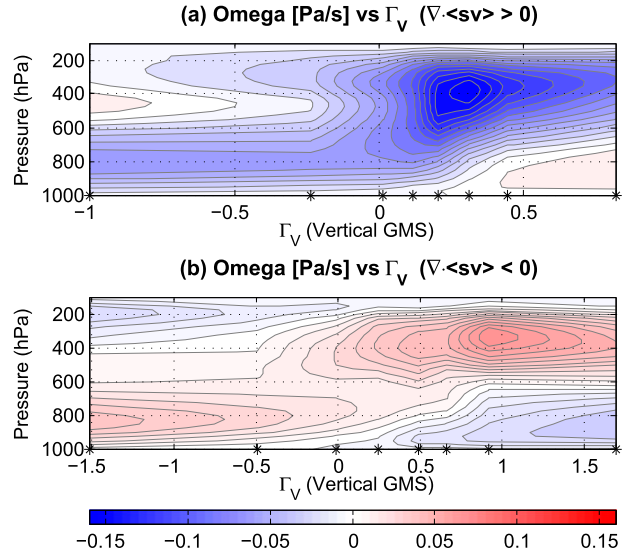


FIG. 6. (a) Vertical ω structures with respect to the values of vertical GMS Γ_V for convectively active times ($\nabla \cdot \langle s\mathbf{v} \rangle > 0$), averaged in 12.5-percentile bins of Γ_V . The star marks on the x axis denote the centers of the bins. (b) As in (a), but for convectively inactive times ($\nabla \cdot \langle s\mathbf{v} \rangle < 0$). The contour interval (CI) of (a) and (b) is $2 \times 10^{-2} \text{ Pa s}^{-1}$. All points with $|\nabla \cdot \langle s\mathbf{v} \rangle|$ less than 10 W m^{-2} were removed to avoid division by zero.

and large Γ_V is associated with bottom-heavy profiles with upper-tropospheric descending motion.

Figure 6b, together with Fig. 6a, completes a life cycle of the convection. The convection is initialized with small and positive Γ_V during negative $\nabla \cdot \langle s\mathbf{v} \rangle$ (in Fig. 6b), and Γ_V increases as the convection develops. After passing the singularity of Γ_V (or zero $\nabla \cdot \langle s\mathbf{v} \rangle$), it becomes a negative and large value that corresponds to bottom-heavy motion (in Fig. 6a), which gradually deepens with increase in Γ_V and reaches the other singularity. Again, the sign of Γ_V flips, and it becomes negative and large when the convection is in a stratiform shape (in Fig. 6b), and, as the stratiform convection is dissipated, the value of Γ_V becomes less negative, completing the life cycle. Since our main interest in this study is convective amplification/decay mechanisms instead of initialization/termination processes, we concentrate on analyses of the data points with positive $\nabla \cdot \langle s\mathbf{v} \rangle$.

Interestingly, the anomalous temperature field is coherent with the ω profiles. Figure 7 shows anomalous temperature profiles with respect to the binned Γ_V , which is compared with Fig. 6a. When Γ_V is negative with bottom-heavy ω profiles, an anomalously warm layer can be observed around 600 hPa. The height of this stable layer matches the upper limit of the bottom-heavy ω . This temperature structure is commonly observed in CCEWs (e.g., Straub and Kiladis 2003; Kiladis et al. 2009; Frierson et al. 2011). We speculate that those

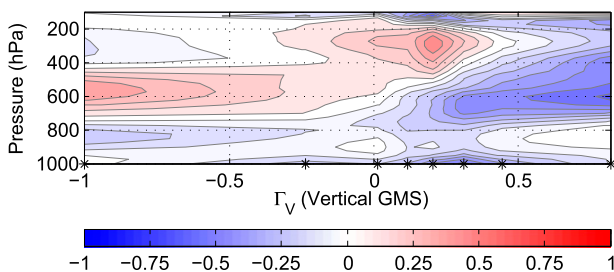


FIG. 7. As in Fig. 6a, but for temperature anomalies (CI = 0.125 K).

temperature anomalies work like a lid that prevents the bottom-heavy ω profiles from becoming top heavy, maintains the negativity of Γ_V , and destabilizes the convective system by enhancing the efficiency of moistening. This type of interaction between temperature anomalies and convection appears to be in favor of the “activation control” hypothesis of large-scale disturbances proposed by [Mapes \(1997\)](#).

Previous TOGA COARE studies (e.g., [Johnson et al. 1996, 1999](#)) have posited that that stable layer is associated with melting processes of cloud droplets around 0°C, though it is not clear why that would occur preferentially during the growth phase of convection. An important role of that layer in convective dynamics has been pointed out by, for instance, [Kikuchi and Takayabu \(2004\)](#), who claimed that moistening below the 0°C level may be an influential factor for development of the convection. However, cloud microphysics may not be the only mechanism for the temperature anomalies. [Raymond et al. \(2014\)](#) claimed that those temperature anomalies are a balanced thermal response to the existence of mesoscale vorticity anomalies in the tropical atmosphere. This hypothesis has been verified in the case of tropical cyclogenesis and in easterly waves (e.g., [Cho and Jenkins 1987; Jenkins and Cho 1991](#)).

d. Critical GMS and feedback constants

Now that we have shown the critical GMS Γ_C stays relatively constant in both the amplifying and decaying phases (in Fig. 5), let us investigate it in more detail. In theoretical GMS studies, where a vertical structure is assumed to be a single mode, the GMS is quasi time independent. That is equivalent to saying that the MSE advection can be linearly parameterized with the intensity of the convection. However, [Inoue and Back \(2015\)](#) demonstrated that the time-independent GMS is not an accurate approximation, especially on 2-day time scales. In this subsection, we will show that linear approximation of the diabatic forcing terms is, instead, more consistent with the observational data during TOGA COARE than that of the advective terms

(cf. Figs. 8c and 8f, which are scatterplots of the diabatic source term F and $\nabla \cdot \langle h\mathbf{v} \rangle$ as a function of $\nabla \cdot \langle s\mathbf{v} \rangle$). This linear approximation of F provides us with a new interpretation of the quasi-time-independent GMS, which will be discussed more in section 5.

Generally, column radiative heating $\langle Q_R \rangle$ can be expressed as

$$\langle Q_R \rangle = r_R LP + Q_0, \quad (17)$$

where r_R is a cloud radiative feedback constant, and Q_0 is the clear-sky column radiative heating (e.g., [Su and Neelin 2002; Bretherton and Sobel 2002; Peters and Bretherton 2005; Sobel 2007](#)). The DSE budget equation [Eq. (4)] with the WTG is

$$\nabla \cdot \langle s\mathbf{v} \rangle \simeq \langle Q_R \rangle + LP. \quad (18)$$

Here, we neglect the surface sensible heat flux. By rearranging Eq. (18) and plugging it into Eq. (17), we obtain

$$\langle Q_R \rangle = \gamma_R \nabla \cdot \langle s\mathbf{v} \rangle + \beta_R, \quad (19)$$

where

$$\gamma_R \equiv \frac{r_R}{1 + r_R} \quad (20)$$

and

$$\beta_R \equiv \frac{Q_0}{1 + r_R}. \quad (21)$$

Figure 8a illustrates a scatterplot of $\langle Q_R \rangle$ versus $\nabla \cdot \langle s\mathbf{v} \rangle$ with the least squares fit; $\langle Q_R \rangle$, which has a high correlation with $\nabla \cdot \langle s\mathbf{v} \rangle$ (0.83), is well represented by the linear equation [Eq. (19)].

Similarly, applying a positive correlation between surface fluxes and precipitation (e.g., [Raymond et al. 2003; Back and Bretherton 2005; Araligidad and Maloney 2008; Riley Dellaripa and Maloney 2015](#)), we obtain

$$S = r_S LP + S_0, \quad (22)$$

where r_S represents an evaporation–moisture convergence feedback (e.g., [Zebiak 1986; Back and Bretherton 2005](#)), and S_0 is the surface fluxes at zero precipitation. In a similar way to Eq. (19), utilizing the DSE budget equation with the WTG, Eq. (22) can be rearranged into

$$S = \gamma_S \nabla \cdot \langle s\mathbf{v} \rangle + \beta_S, \quad (23)$$

where

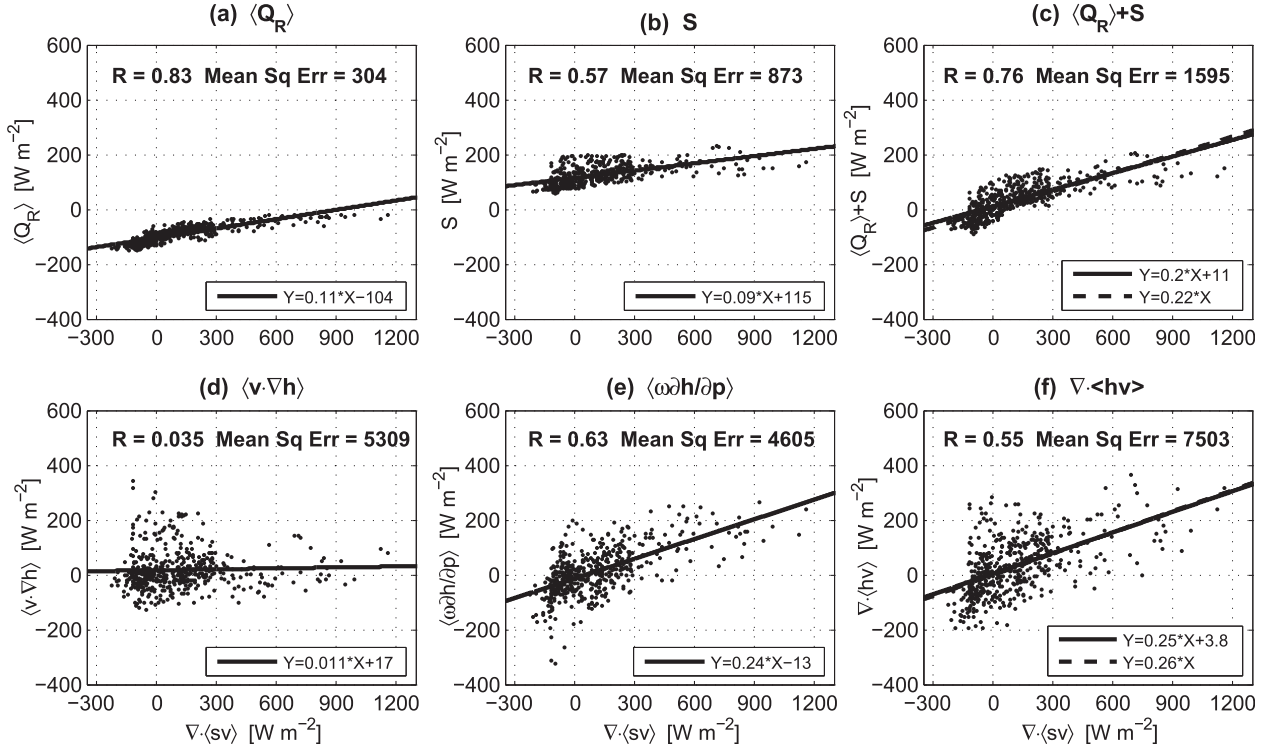


FIG. 8. (a) Scatterplot of column radiative heating $\langle Q_R \rangle$ as a function of vertically integrated total DSE export ($+\nabla \cdot \langle s\mathbf{v} \rangle$) for all data points, including convectively inactive times. The solid line was computed by the linear least squares fitting. The values in the upper-left corner represent correlation coefficient R and mean-square error (Mean Sq Err) from the linear fit. (b)–(f) As in (a), but for (b) surface fluxes S , (c) diabatic forcing $\langle Q_R \rangle + S$, (d) vertically integrated horizontal MSE export ($+\langle \mathbf{v} \cdot \nabla h \rangle$), (e) vertically integrated vertical MSE export ($+\langle \omega \partial h / \partial p \rangle$), and (f) the total MSE export ($+\nabla \cdot \langle h\mathbf{v} \rangle$). The dashed lines in (c) and (f) were computed by a regression through the origin.

$$\gamma_S \equiv \frac{r_S}{1 + r_R} \quad (24)$$

and

$$\beta_S \equiv \frac{S_0 + r_R S_0 - r_S Q_0}{1 + r_R}. \quad (25)$$

Figure 8b is a scatterplot of S versus $\nabla \cdot \langle s\mathbf{v} \rangle$ with the least squares fit. The linear fit seems adequate enough to express the overall pattern of S . As pointed out by previous studies, there is a positive correlation (0.57) between S and intensity of the convection ($\nabla \cdot \langle s\mathbf{v} \rangle$ in this study). However, this positive correlation is not the only reason for the validity of the linear approximation of S , because the correlation between $\nabla \cdot \langle h\mathbf{v} \rangle$ and $\nabla \cdot \langle s\mathbf{v} \rangle$ is also high (0.55) and is comparable to that of S . [The correlation of $\langle \omega \partial h / \partial p \rangle$ is even higher (0.63).] For the linear approximation of S to be more accurate than that of $\nabla \cdot \langle h\mathbf{v} \rangle$, besides the positive correlation, small variance of S compared to the other MSE budget terms (especially $\nabla \cdot \langle h\mathbf{v} \rangle$) is required. That can be seen in the

values of the mean-square errors of the linear fits given in Fig. 8. The mean-square error for S is about an order smaller than that for $\nabla \cdot \langle h\mathbf{v} \rangle$, indicating that the linear fit of S is better than that of $\nabla \cdot \langle h\mathbf{v} \rangle$. This smaller mean-square error is simply as a result of the smaller variance of S than that of $\nabla \cdot \langle h\mathbf{v} \rangle$.

Hence, for Eq. (23) to be more valid than assuming a constant GMS, two conditions have to be satisfied: 1) S is positively correlated with $\nabla \cdot \langle s\mathbf{v} \rangle$, and 2) variance of S is much smaller than that of $\nabla \cdot \langle h\mathbf{v} \rangle$. The second condition is violated in longer time scales, such as the MJO scale, in which variance of S is comparable to the other MSE budget terms (e.g., Maloney 2009; Benedict et al. 2014; Inoue and Back 2015). Furthermore, Riley Dellaripa and Maloney (2015) found that the relationship between S and convective intensity [or γ_S in Eq. (23)] significantly varies along a life cycle of the MJO. It must be noted, therefore, that, although the same methodology we used in this work (drying efficiency composite) is applicable to the search for moistening/drying mechanisms in MJO events, the potential conclusions for the MJO are likely to be different from the conclusions in this study. For

instance, we can make a similar figure to Fig. 5 for the MJO. In that figure, however, Γ_C is most likely not nearly constant because of the significant variation of γ_S in Eq. (23) along an MJO life cycle. We more thoroughly discuss time-scale dependency and what time scales we are seeing the behavior of in this study in section 4g.

Since both $\langle Q_R \rangle$ and S are well represented by the least squares fit, this is also the case for F , the combination of $\langle Q_R \rangle$ and S . Adding Eqs. (19) and (23) yields

$$F \equiv \langle Q_R \rangle + S = \gamma \nabla \cdot \langle s\mathbf{v} \rangle + \beta, \quad (26)$$

where

$$\gamma \equiv \gamma_R + \gamma_S = \frac{r_R + r_S}{1 + r_R} \quad (27)$$

and

$$\beta \equiv \beta_R + \beta_S = \frac{Q_0 + S_0 + r_R S_0 - r_S Q_0}{1 + r_R}, \quad (28)$$

which is shown in Fig. 8c with a high correlation coefficient (0.76).

Interestingly, Eq. (26) can be simplified further because, in the TOGA COARE data, the intercept of the $\langle Q_R \rangle$ fitting (β_R ; in Fig. 8a) cancels out the intercept of the S fitting (β_S ; in Fig. 8b), causing the intercept of the F fitting (β ; in Fig. 8c) to be negligible. Hence, Eq. (26) becomes

$$F \simeq \gamma \nabla \cdot \langle s\mathbf{v} \rangle. \quad (29)$$

Therefore, the critical GMS is

$$\Gamma_C \equiv \frac{F}{\nabla \cdot \langle s\mathbf{v} \rangle} \simeq \gamma. \quad (30)$$

The good linear fit of F indicates the constancy of Γ_C in Fig. 5 in the TOGA COARE dataset. (Of course, this linear approximation is not perfect, and, thus, Γ_C slightly varies in Fig. 5.) The amplifying and decaying phases, Eqs. (12) and (13), can be written as

$$\Gamma - \gamma < 0 \quad \text{and} \quad (31)$$

$$\Gamma - \gamma > 0. \quad (32)$$

These equations suggest that a convective system intensifies (decays) if the GMS is less (greater) than the feedback constant γ . Thus, how much convection can grow is tightly related to the feedback constant γ .

We do not yet understand why the intercept is close to zero. It would be interesting to examine whether this disappearance of the intercept β is just a coincidence or is due to some physical constraints. Although we are not

sure if this is the case in general, we could, at least, use simple linearization [Eq. (29)] in a simple model framework, the implications of which will be discussed in section 5.

When dealing with anomalous MSE budgets instead of the total budgets, the argument becomes much simpler, because we do not have to worry about the intercept β . We can take anomalies of the MSE budgets to obtain similar relations to Eqs. (31) and (32), as follows:

$$\Gamma' - \gamma < 0 \quad \text{and} \quad (33)$$

$$\Gamma' - \gamma > 0, \quad (34)$$

where

$$\Gamma' \equiv \frac{\nabla \cdot \langle h\mathbf{v} \rangle'}{\nabla \cdot \langle s\mathbf{v} \rangle'} \quad (35)$$

is anomalous GMS. [Interpretations of the anomalous GMS are discussed in Inoue and Back (2015).] Equations (33) and (34), respectively, correspond to the amplifying and decaying phases, and precipitation reaches the maximum when

$$\Gamma'|_{P_{\max}} = \gamma. \quad (36)$$

In spite of the simplicity of the anomalous form, we include the mean state in our argument below in order to obtain further interesting ideas discussed in section 5.

Before going to the next subsection, it should be acknowledged that the arguments given above are just statistical ones and are not based on physical reasoning. In other words, we have not discussed a priori reasons why, for instance, S has a positive linear relationship with the convective intensity. It might be because of downdraft-enhanced gustiness (Redelsperger et al. 2000) or a convergence feedback, where enhanced surface fluxes lead to enhanced precipitation, but examining these a priori reasons is beyond the scope of this study, and more thorough studies about those are required for more general conclusions.

e. Drying efficiency and convective structures

We have thus far shown the following:

- Bottom heaviness of ω associated with negative vertical GMS Γ_V is responsible for most of the moisture (or MSE) import in the amplifying phase.
- That bottom heaviness might be related to middle-tropospheric temperature anomalies.
- In the amplifying phase, horizontal GMS Γ_H is close to zero, indicating a small contribution of the horizontal advection to the moistening.

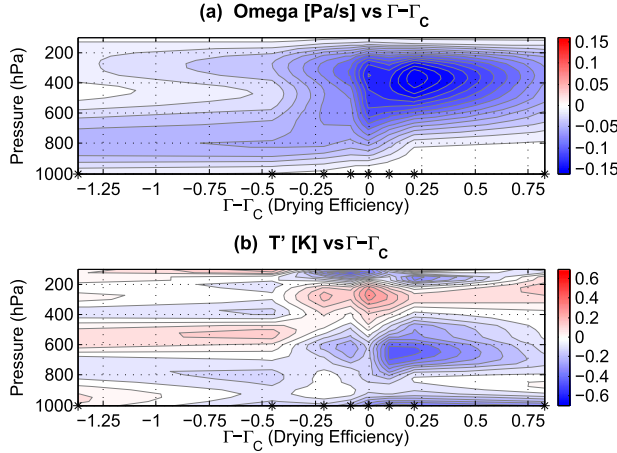


FIG. 9. (a) Binned vertical ω structures with respect to the drying efficiency $\Gamma - \Gamma_c$ for convectively active times ($\nabla \cdot \langle \mathbf{s}\mathbf{v} \rangle > 0$), averaged in the same bins as in Figs. 4 and 5 ($CI = 2 \times 10^{-2} \text{ Pa s}^{-1}$). The star marks on the x axis denote the bin centers. (b) As in (a), but for temperature anomalies ($CI = 0.1 \text{ K}$).

- Critical GMS Γ_c is broadly constant because of the linearity of $\langle Q_R \rangle$ and S and because of the cancellation of the intercept β .
- In the decaying phase, both vertical and horizontal advection export column moisture (i.e., $\Gamma_H, \Gamma_V > 0$), but the horizontal advection exports more efficiently (i.e., $\Gamma_H > \Gamma_V$).

Those points are summarized in Figs. 9 and 10, which illustrate vertical structures of ω , temperature anomalies, and vertical and horizontal MSE advection as a function of the binned $\Gamma - \Gamma_c$.

When $\Gamma - \Gamma_c$ is negative, ω is in a bottom-heavy shape (Fig. 9a) which imports MSE from the lower troposphere (Fig. 10a), whereas the horizontal advection plays only a little role in the moistening processes in this phase (Fig. 10b). The bottom heaviness of ω might be related to the anomalously warm layer at about 600 hPa, observed in Fig. 9b. Since Γ_c is broadly constant, it does not change the vertical structures, but it contributes to the shift of the x axis compared to Fig. 6a. For instance, in Fig. 6a, ω starts to become top heavy at $\Gamma_V \simeq -0.25$, whereas in Fig. 9a it does at $\Gamma - \Gamma_c \simeq -0.45$. The difference between those values is due to Γ_c , which is roughly constant.

When $\Gamma - \Gamma_c$ is positive, ω with a top-heavy shape (Fig. 9a) exports MSE from the upper troposphere (Fig. 10a). Besides that, horizontal advection also exports MSE from the lower to middle troposphere, as depicted in Fig. 10b. This behavior of the horizontal advection is not surprising. Generally, at the very end of the dissipative stage of convection, the atmospheric column is anomalously moist compared to the surrounding environment. Therefore, horizontal winds in

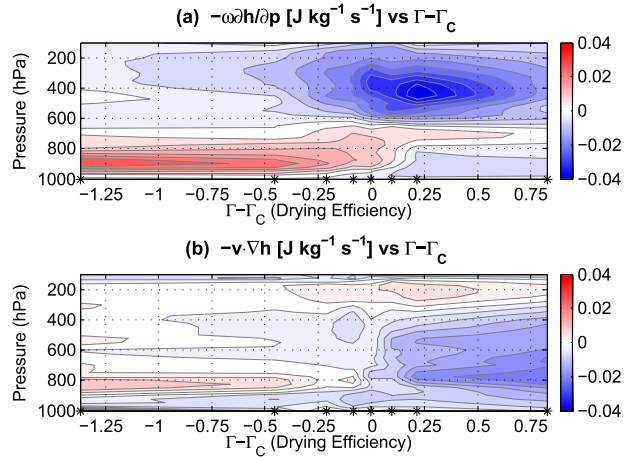


FIG. 10. As in Fig. 9, but for (a) vertical and (b) horizontal MSE advection ($CI = 5 \times 10^{-3} \text{ J kg}^{-1} \text{ s}^{-1}$).

any direction lead to drying of the atmospheric column, causing positive Γ_H , as shown in Fig. 10b.

The mechanisms described above imply that tropical convection is a self-regulating system. Variability of the drying efficiency is predominantly regulated by the shape of vertical velocity profiles (in the amplifying phase) and by the atmospheric column moisture (in the decaying phase), both of which are parts of the convective system. Moreover, timing of a transition from the amplifying into the decaying phase is associated with the feedback constants between the radiation, the evaporation, and the convection. A convective episode that starts with shallow convection spontaneously enhances the convection itself via bottom-heavy ω . Deepened convection, in turn, starts to dry out the system via top-heavy ω , dissipating the convection. In the decaying phase, horizontal winds also dry the system by carrying dry air from the surrounding environment into the convective system or carrying moist air from the system to the environment. Therefore, we might be able to refer to the amplifying (decaying) phases as “self-amplifying (self-decaying)” phases.

f. Vertical structures and resulting convective intensity

Now we investigate a qualitative relationship between vertical structures and resulting convective intensity. Utilizing the MSE budget equation [Eq. (6)] and the linearized precipitation equation [Eq. (8)], we obtain the following:

$$\tau_c \frac{\partial LP}{\partial t} = -\nabla \cdot \langle h\mathbf{v} \rangle + F. \quad (37)$$

Dividing both sides by $\nabla \cdot \langle \mathbf{s}\mathbf{v} \rangle$ and applying Eqs. (17) and (18) yields

$$\frac{\partial \ln(LP + \beta_R)}{\partial t} = -\frac{r_R + 1}{\tau_c}(\Gamma - \Gamma_C), \quad (38)$$

where r_R and β_R are the constants defined in Eq. (19). We neglect the sensible heat flux. This equation is only applicable to the data points with positive $\nabla \cdot \langle s\mathbf{v} \rangle$. We solve this equation for P and obtain

$$LP = (LP_0 + \beta_R) \exp\left(\frac{r_R + 1}{\tau_c} \Lambda\right) - \beta_R, \quad (39)$$

where

$$\Lambda \equiv - \int_{t_0}^t (\Gamma - \Gamma_C) dt,$$

and P_0 and t_0 are some reference precipitation and time. This equation demonstrates that the rate of precipitation increase is determined by Λ , a time integration of the efficiency of moistening (negative drying efficiency). There are three ways to increase Λ : 1) decrease Γ via bottom-heavy ω ; 2) increase Γ_C via enhanced feedbacks between the convection, the radiation, and the evaporation [according to Eqs. (27) and (30)]; and 3) increase the duration in which $\Gamma - \Gamma_C$ is negative. Therefore, bottom-heavy ω , strong radiative–cloud and evaporation–convergence feedbacks, and a long duration of shallower vertical motion profiles can all intensify the resulting precipitation maximum. In Figs. 7 and 9b, we observed the temperature anomalies in the middle troposphere that might maintain the bottom heaviness of ω . Hence, it would be interesting to test whether there is a positive correlation between the intensity of the temperature anomalies and the intensity of the resulting convection.

g. Time-scale dependence

When examining MSE budgets in tropical variability, it is always necessary to clarify which time scale is the target, because MSE budgets behave in significantly different ways between different time scales (e.g., Inoue and Back 2015). In this study, we have taken composites with respect to the values of $\Gamma - \Gamma_C$, which are, according to Eq. (15), equivalent to negative column water vapor tendency per unit intensity of the convection. Therefore, it is natural to think that our analyses herein represent the convective structures with the highest frequency in the dataset. We have removed the diurnal cycle; thus, the highest-frequency variability in the TOGA COARE data is disturbance with ~ 2 -day periodicity (see Fig. 1 in Inoue and Back 2015). We examined the structures of the high-frequency disturbances using the same data (not shown) and found significant

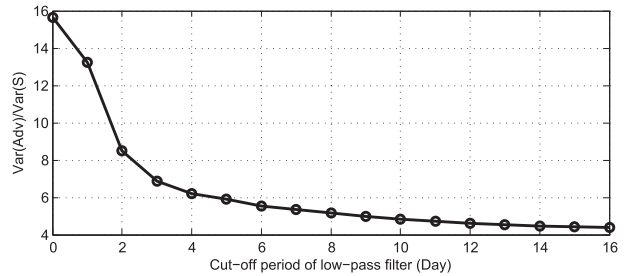


FIG. 11. Ratio of the variance of $\nabla \cdot \langle h\mathbf{v} \rangle$ to the variance of S on different time scales. The x axis represents the cutoff period of the low-pass Lanczos filter with 151 weights, and the y axis represents the ratio of $\text{var}(\nabla \cdot \langle h\mathbf{v} \rangle)$ to $\text{var}(S)$.

resemblances with the structures shown in Figs. 6, 7, 9, and 10.

By using a low-pass (or bandpass) filter, we could apply this method to lower-frequency variability, such as Kelvin waves and the MJO. In section 4d, however, we showed that the linear approximation of S requires small variance of S compared with $\nabla \cdot \langle h\mathbf{v} \rangle$, and that condition is violated as the time scale gets longer. Figure 11 illustrates the ratio of the variance of $\nabla \cdot \langle h\mathbf{v} \rangle$ to the variance of S as a function of cutoff period of the Lanczos low-pass filter with 151 weights. This figure shows the same information as the ratio of power spectra between them. As the cutoff period increases, the periodicity of the time series becomes longer. This figure shows that, as the periodicity becomes longer, the variance of $\nabla \cdot \langle h\mathbf{v} \rangle$, which dominates S on short time scales, becomes more comparable to the variance of S . It indicates that the linear approximation of S becomes less accurate on longer time scales; thus, we cannot assume the constancy of the critical GMS Γ_C any more.

We have discussed the convective amplification/decay mechanisms in such a way that, because Γ_C is nearly constant, variability of Γ is the most important. But this may not be the case for longer-time-scale disturbances, such as the MJO. Therefore, although a similar methodology is applicable to the MJO, the potential conclusions may be different from that in this study. It would be interesting to perform a similar analysis to that here for longer time scales of variability.

5. More discussion: Characteristic GMS

As described above, the gross moist stability Γ is a highly time-dependent quantity, which significantly varies from negative to positive along the convective life cycle. Recent diagnostic studies have focused more on the time-dependent aspect of Γ (e.g., Hannah and Maloney 2011; Benedict et al. 2014; Hannah and Maloney 2014; Masunaga and L'Ecuyer 2014; Sobel

et al. 2014; Inoue and Back 2015); on the other hand, quasi-time-independent GMS has been popularly utilized in theoretical studies (e.g., Neelin and Held 1987; Emanuel et al. 1994; Neelin and Yu 1994; Tian and Ramanathan 2003; Fuchs and Raymond 2007; Raymond et al. 2009; Sugiyama 2009; Sobel and Maloney 2012). Then, some natural questions will come up: How can we calculate a meaningful value of the quasi-time-independent GMS in observational data, how can we interpret it, and how can we relate it with the highly time-dependent GMS? Fortunately, all the analyses shown so far in this paper have already provided the answers for those questions. We will clarify those answers through a couple steps.

First, we need to clarify how to calculate a single meaningful value of the quasi-time-independent GMS. There have been a couple different ways proposed from different contexts. We now show that all of them are almost equivalent in the TOGA COARE dataset. Those different definitions are listed as follows:

- (i) GMS defined at the maximum anomalous precipitation (e.g., Sobel and Bretherton 2003), or

$$\Gamma'_{\max} \equiv \Gamma'|_{P_{\max}}; \quad (40)$$

- (ii) GMS computed from a scatterplot of anomalous $\nabla \cdot \langle h\mathbf{v} \rangle$ versus $\nabla \cdot \langle s\mathbf{v} \rangle$ [e.g., Table 1 in Inoue and Back (2015)], or

$$\tilde{\Gamma}' \equiv \frac{\overline{\nabla \cdot \langle h\mathbf{v} \rangle' \times \nabla \cdot \langle s\mathbf{v} \rangle'}}{\overline{\nabla \cdot \langle s\mathbf{v} \rangle'^2}}; \quad (41)$$

- (iii) GMS computed from a scatterplot of nonanomalous $\nabla \cdot \langle h\mathbf{v} \rangle$ versus $\nabla \cdot \langle s\mathbf{v} \rangle$ [e.g., Fig. 9 in Raymond and Fuchs (2009)], or

$$\tilde{\Gamma} \equiv \frac{\overline{\nabla \cdot \langle h\mathbf{v} \rangle \times \nabla \cdot \langle s\mathbf{v} \rangle}}{\overline{\nabla \cdot \langle s\mathbf{v} \rangle^2}}; \quad (42)$$

- (iv) climatological GMS [e.g., Eq. (7) in Kuang (2011)], or

$$\Gamma_0 \equiv \frac{\overline{\nabla \cdot \langle h\mathbf{v} \rangle}}{\overline{\nabla \cdot \langle s\mathbf{v} \rangle}}; \quad (43)$$

The overbar represents time average, and the prime is perturbation from the time mean. There are a few more different methods to estimate quasi-time-independent GMS (e.g., Yu et al. 1998; Chou et al. 2013), but all of them can be qualitatively categorized in one of the above definitions. We include the horizontal advection

in the definitions above, although it is generally not included.

From Eq. (36), Γ'_{\max} is equal to γ , which represents a combination of the radiative–convective and the evaporation–convergence feedback constants according to Eq. (27). Now, γ can be statistically calculated by a least squares method as

$$\gamma = \frac{\overline{F' \times \nabla \cdot \langle s\mathbf{v} \rangle'}}{\overline{\nabla \cdot \langle s\mathbf{v} \rangle'^2}}. \quad (44)$$

But from the MSE budget equation, γ is also expressed as

$$\gamma = \frac{\overline{(\partial \langle h \rangle / \partial t + \nabla \cdot \langle h\mathbf{v} \rangle') \times \nabla \cdot \langle s\mathbf{v} \rangle'}}{\overline{\nabla \cdot \langle s\mathbf{v} \rangle'^2}}. \quad (45)$$

Since $\partial \langle h \rangle / \partial t$ and $\nabla \cdot \langle s\mathbf{v} \rangle'$ (or P') are almost out of phase (e.g., Inoue and Back 2015), covariance between them becomes negligible if the time series is long enough. Therefore, we obtain

$$\Gamma'_{\max} = \gamma = \tilde{\Gamma}'. \quad (46)$$

Moreover, in the TOGA COARE data, the intercept of the least squares fit of F (β ; in Fig. 8c) is negligible. This indicates that the least squares fit of $\nabla \cdot \langle h\mathbf{v} \rangle$ as a function of $\nabla \cdot \langle s\mathbf{v} \rangle$ also has to go through the origin, as shown in Fig. 8f, where the least squares fit is almost identical to the regression line through the origin. Therefore, we obtain

$$\tilde{\Gamma}' = \tilde{\Gamma}, \quad (47)$$

and this equation can be rearranged into

$$\tilde{\Gamma}' = \Gamma_0. \quad (48)$$

Furthermore, Fig. 8d shows the horizontal component of $\tilde{\Gamma}'$, $\tilde{\Gamma}'_H$, is close to zero (0.011); hence,

$$\tilde{\Gamma}' \simeq \tilde{\Gamma}'_V, \quad (49)$$

where $\tilde{\Gamma}'_V$ is the vertical component of $\tilde{\Gamma}'$.

The above arguments demonstrate that all the quasi-time-independent GMSs defined in the different ways (i)–(iv) are equivalent and are all equal to γ in the TOGA COARE data. We collectively call them the characteristic GMS. From the definition of γ [Eq. (27)], it represents a combination of the radiative–convective and the evaporation–convergence feedback constants, and, moreover, it is equal to the critical GMS Γ_C from Eq. (30), which is the threshold between the amplifying and the decaying phases [Eqs. (12) and (13)]. Therefore,

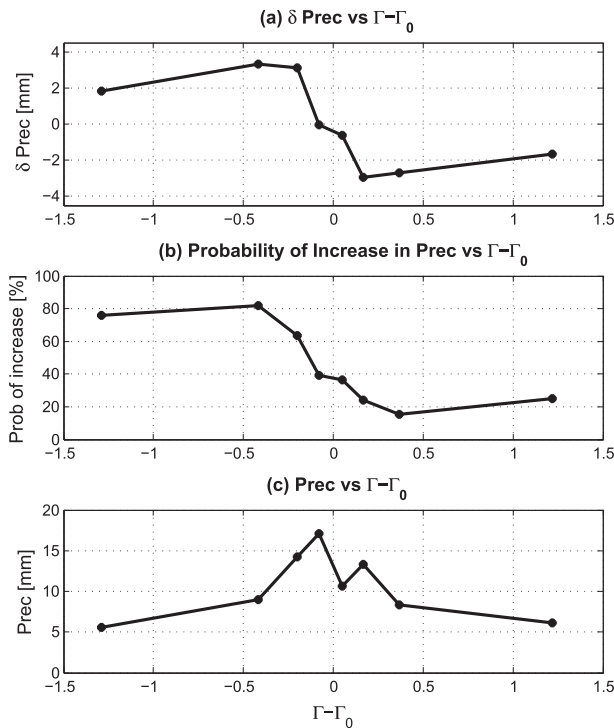


FIG. 12. As in Fig. 4, but as a function of GMS minus climatological GMS $\Gamma - \Gamma_0$.

we can interpret all the characteristic GMSs, Γ'_{\max} , $\tilde{\Gamma}'$, $\tilde{\Gamma}$, and Γ_0 , as follows:

- 1) a critical value that determines the threshold between the amplifying and the decaying phases of the convection at a given place;
- 2) a value of the time-dependent GMS at the precipitation maximum;
- 3) a combination of the radiative–convective and the evaporation–convergence feedback constants.

These interpretations are useful for clarifying the mechanisms for convective amplification/decay. At a given place, convection intensifies if a value of the time-dependent GMS is below the characteristic (or climatological) GMS at that place, and subcritical GMS is primarily because of bottom-heavy ω profiles. Eventually, the ω profile becomes a top-heavy shape, causing the GMS to be greater than the critical value, which leads to decay of the convection. This idea is demonstrated in Fig. 12. Here, Γ_c in Fig. 4 is replaced with the climatological GMS Γ_0 . The figure shows that, when $\Gamma - \Gamma_0$ is negative (positive), the convection intensifies (decays) as shown in Fig. 4. This mechanism is consistent with what Masunaga and L'Ecuyer (2014) claimed. Furthermore, the third interpretation indicates that the feedback constant γ ($\equiv \gamma_R + \gamma_S$) is equal to the

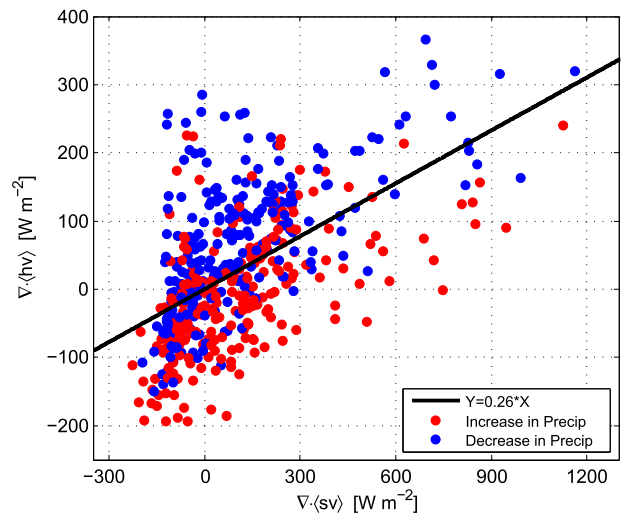


FIG. 13. Scatterplot of $\nabla \cdot \langle \mathbf{hv} \rangle$ vs $\nabla \cdot \langle \mathbf{sv} \rangle$ with the characteristic (or climatological) GMS line as in Fig. 8f. The dots represent data points when the precipitation increases (red) and decreases (blue).

climatological GMS Γ_0 , which is primarily determined by climatological ω profiles. That relationship implies a tight connection between ω profile shapes and the linear feedback mechanisms between the radiation, the evaporation, and the convection.

For facilitating conceptualization of the GMS variability, Fig. 12 is plotted in a different plane. In Fig. 13, the red (blue) dots represent data points in which convection intensifies (decays), and the slope of the black solid line represents the characteristic (or critical, or climatological) GMS. This figure illustrates that, when a dot is located below (above) the critical line in this plane [which is equivalent to negative (positive) drying efficiency], the convection intensifies (decays). Since the x axis represents convective intensity, as convection develops, the dot moves to the right. But the GMS has to be equal to the climatological one at the convective maximum. So the dot also moves toward the characteristic GMS line. This idea is depicted in Fig. 14. From this figure, we can view each short-time-scale convective life cycle as a fluctuation of the rapidly varying GMS (shown in the thin light red arrows) around the slowly varying climatological GMS line (shown as the solid blue line) in the $\nabla \cdot \langle \mathbf{hv} \rangle$ -versus- $\nabla \cdot \langle \mathbf{sv} \rangle$ plane. In this study, we utilized the rapidly varying property of the GMS (shown in the thick red arrow) to extract the mechanisms for convective application/decay, ignoring the slow variation (shown in the thick blue arrows) of the climatological GMS, which is regulated by large-scale phenomena, such as a planetary boundary layer contribution controlled by SST gradient (e.g., Sobel and Neelin 2006; Back and Bretherton 2009a,b).

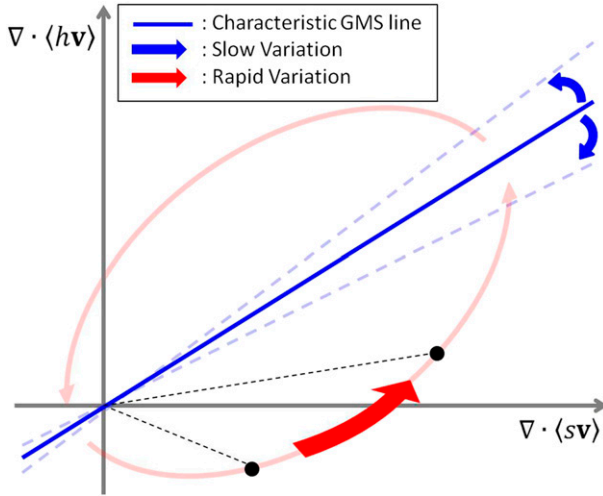


FIG. 14. Schematic figure of a convective life cycle (light red arrows) in the $\nabla \cdot \langle h \mathbf{v} \rangle$ -vs- $\nabla \cdot \langle s \mathbf{v} \rangle$ plane. The thick red arrow represents variation of highly time-dependent GMS; the thick blue arrows represent variation of slowly changing climatological GMS.

6. Summary

We have investigated the convective amplification/decay mechanisms in short-time-scale disturbances by examining the gross moist stability (GMS; Γ) and its relevant quantities in the TOGA COARE dataset. We coined two quantities: namely, the critical GMS Γ_C and the drying efficiency $\Gamma - \Gamma_C$. The drying efficiency is a version of the effective GMS, which represents negative precipitable water tendency per unit intensity of convection. The GMS Γ and critical GMS Γ_C , respectively, represent the contributions of the advective terms ($\nabla \cdot \langle h \mathbf{v} \rangle$) and the diabatic forcing terms ($F \equiv \langle Q_R \rangle + S$) to the drying efficiency.

First, we verified that the convection is amplified (attenuated) via negative (positive) drying efficiency; Figs. 4a and 4b show that the precipitation intensifies (decays) when $\Gamma - \Gamma_C$ is negative (positive). Therefore, we call the phases with negative (positive) $\Gamma - \Gamma_C$ the amplifying (decaying) phases. We also found that the precipitation reaches the maximum when $\Gamma - \Gamma_C$ is zero, or the GMS is equal to the critical GMS (Fig. 4c).

Next, we investigated which processes explain the variability of $\Gamma - \Gamma_C$. By doing so, we can clarify which processes destabilize the convection and how the convection is forced to transition from the amplifying into the decaying phases. In the amplifying phase (i.e., $\Gamma - \Gamma_C < 0$), most of the variability of $\Gamma - \Gamma_C$ is explained by the vertical GMS Γ_V (Fig. 5), which indicates that the convective transition from the amplifying into the decaying phases is primarily controlled by the vertical MSE advection. Convection with a bottom-heavy

ω profile efficiently imports MSE via low-level convergence (negative Γ_V), which leads to further enhancement of the convection via column moistening. Positive temperature anomalies in the middle troposphere might play a role in controlling the bottom heaviness of ω . As the convection develops, the ω profile gradually becomes top heavy, starting export of the column MSE from the upper troposphere (positive Γ_V), which leads to dissipation of the convection, finishing the amplifying phase. During the amplifying phase, the horizontal GMS Γ_H broadly stays close to zero, indicating that the horizontal MSE advection does not contribute the column moistening in this phase. In the decaying phase ($\Gamma - \Gamma_C < 0$), in contrast, the variability of $\Gamma - \Gamma_C$ is mainly explained by Γ_H . In this phase, the vertical advection also exports MSE (i.e., $\Gamma_V > 0$), but the horizontal advection exports more efficiently (i.e., $\Gamma_H > \Gamma_V$), leading to decay of the convection via column drying.

Throughout the convective life cycle, the critical GMS Γ_C broadly stays constant with positive values (Fig. 5). This indicates that the column radiative heating and surface fluxes always tend to destabilize the convective system by supplying the MSE sources in a constant manner. The constancy of Γ_C is due to the linearity of the diabatic forcing with respect to the intensity of the convection (which is the case only in short-time-scale disturbances), and also due to the disappearance of the intercept β in Eq. (26). Although we are not sure whether or not the negligible β is the case in general, the linear approximation of the diabatic forcing provides us with a simple framework in which we can interpret the GMS in novel ways.

In section 5, we extended our arguments toward the quasi-time-independent GMS. We demonstrated that all of the following definitions of the quasi-time-independent GMSs are equivalent in the TOGA COARE data: (i) anomalous GMS at the precipitation maximum (Γ'_{\max}), (ii) GMS computed from a scatterplot of anomalous $\nabla \cdot \langle h \mathbf{v} \rangle$ versus $\nabla \cdot \langle s \mathbf{v} \rangle$ ($\bar{\Gamma}'$), (iii) GMS computed from a scatterplot of nonanomalous $\nabla \cdot \langle h \mathbf{v} \rangle$ versus $\nabla \cdot \langle s \mathbf{v} \rangle$ ($\bar{\Gamma}$), and (iv) climatological GMS (Γ_0), all of which are collectively called the characteristic GMS. The characteristic GMS can be interpreted as 1) a critical value that determines the threshold between the amplifying and the decaying phases, 2) a value of the GMS at the precipitation maximum, and 3) a combination of the radiative-convective and the evaporation-convergence feedback constants. These interpretations, together with Fig. 14, facilitate conceptualization of the GMS variability. From this figure, we can view a short-time-scale convective life cycle as a fluctuation of rapidly changing GMS around a slowly changing climatological GMS line in the $\nabla \cdot \langle h \mathbf{v} \rangle$ -versus- $\nabla \cdot \langle s \mathbf{v} \rangle$ plane. In this

study, we utilized the rapidly changing property of the GMS to diagnose the convective amplification/decay mechanisms.

Acknowledgments. We thank Professor Gregory J. Tripoli and Professor Matthew H. Hitchman for reading Kuniaki Inoue's M.S. thesis describing a part of this study. We also thank Professor Adam H. Sobel, Professor David J. Raymond, and one anonymous reviewer for their constructive comments that improved our first manuscript significantly. We are grateful to Professor Minghua Zhang, who has made his TOGA COARE dataset publicly available. This research is supported by NASA Grant NNX12AL96G.

REFERENCES

- Araligidad, N. M., and E. D. Maloney, 2008: Wind-driven latent heat flux and the intraseasonal oscillation. *Geophys. Res. Lett.*, **35**, L04815, doi:[10.1029/2007GL032746](#).
- Back, L. E., and C. S. Bretherton, 2005: The relationship between wind speed and precipitation in the Pacific ITCZ. *J. Climate*, **18**, 4317–4328, doi:[10.1175/JCLI3519.1](#).
- , and —, 2006: Geographic variability in the export of moist static energy and vertical motion profiles in the tropical Pacific. *Geophys. Res. Lett.*, **33**, L17810, doi:[10.1029/2006GL026672](#).
- , and —, 2009a: On the relationship between SST gradients, boundary layer winds, and convergence over the tropical oceans. *J. Climate*, **22**, 4182–4196, doi:[10.1175/2009JCLI2392.1](#).
- , and —, 2009b: A simple model of climatological rainfall and vertical motion patterns over the tropical oceans. *J. Climate*, **22**, 6477–6497, doi:[10.1175/2009JCLI2393.1](#).
- Benedict, J. J., E. D. Maloney, A. H. Sobel, D. M. W. Frierson, and L. J. Donner, 2013: Tropical intraseasonal variability in version 3 of the GFDL Atmosphere Model. *J. Climate*, **26**, 426–449, doi:[10.1175/JCLI-D-12-00103.1](#).
- , —, —, and —, 2014: Gross moist stability and MJO simulation skill in three full-physics GCMs. *J. Atmos. Sci.*, **71**, 3327–3349, doi:[10.1175/JAS-D-13-0240.1](#).
- Betts, A. K., 1986: A new convective adjustment scheme. Part I: Observational and theoretical basis. *Quart. J. Roy. Meteor. Soc.*, **112**, 677–691, doi:[10.1002/qj.49711247307](#).
- , and M. J. Miller, 1986: A new convective adjustment scheme. Part II: Single column tests using GATE wave, BOMEX, ATEX and arctic air-mass data sets. *Quart. J. Roy. Meteor. Soc.*, **112**, 693–709, doi:[10.1002/qj.49711247308](#).
- Bretherton, C. S., and P. K. Smolarkiewicz, 1989: Gravity waves, compensating subsidence and detrainment around cumulus clouds. *J. Atmos. Sci.*, **46**, 740–759, doi:[10.1175/1520-0469\(1989\)046<0740:GWCSAD>2.0.CO;2](#).
- , and A. H. Sobel, 2002: A simple model of a convectively coupled Walker circulation using the weak temperature gradient approximation. *J. Climate*, **15**, 2907–2920, doi:[10.1175/1520-0442\(2002\)015<2907:ASMOAC>2.0.CO;2](#).
- , M. E. Peters, and L. E. Back, 2004: Relationships between water vapor path and precipitation over the tropical oceans. *J. Climate*, **17**, 1517–1528, doi:[10.1175/1520-0442\(2004\)017<1517:RBWVPA>2.0.CO;2](#).
- Charney, J. G., 1963: A note on large-scale motions in the tropics. *J. Atmos. Sci.*, **20**, 607–609, doi:[10.1175/1520-0469\(1963\)020<0607:ANOLSM>2.0.CO;2](#).
- , 1969: A further note on large-scale motions in the tropics. *J. Atmos. Sci.*, **26**, 182–185, doi:[10.1175/1520-0469\(1969\)026<0182:AFNOLS>2.0.CO;2](#).
- Cho, H.-R., and M. A. Jenkins, 1987: The thermal structure of tropical easterly waves. *J. Atmos. Sci.*, **44**, 2531–2539, doi:[10.1175/1520-0469\(1987\)044<2531:TTSOTE>2.0.CO;2](#).
- Chou, C., T.-C. Wu, and P.-H. Tan, 2013: Changes in gross moist stability in the tropics under global warming. *Climate Dyn.*, **41**, 2481–2496, doi:[10.1007/s00382-013-1703-2](#).
- Emanuel, K. A., J. D. Neelin, and C. S. Bretherton, 1994: On large-scale circulations in convecting atmospheres. *Quart. J. Roy. Meteor. Soc.*, **120**, 1111–1143, doi:[10.1002/qj.49712051902](#).
- Frierson, D. M. W., D. Kim, I.-S. Kang, M.-I. Lee, and J. Lin, 2011: Structure of AGCM-simulated convectively coupled Kelvin waves and sensitivity to convective parameterization. *J. Atmos. Sci.*, **68**, 26–45, doi:[10.1175/2010JAS3356.1](#).
- Fuchs, Z., and D. J. Raymond, 2007: A simple, vertically resolved model of tropical disturbances with a humidity closure. *Tellus*, **59A**, 344–354, doi:[10.1111/j.1600-0870.2007.00230.x](#).
- , S. Gjorgjievska, and D. J. Raymond, 2012: Effects of varying the shape of the convective heating profile on convectively coupled gravity waves and moisture modes. *J. Atmos. Sci.*, **69**, 2505–2519, doi:[10.1175/JAS-D-11-0308.1](#).
- Hannah, W. M., and E. D. Maloney, 2011: The role of moisture–convection feedbacks in simulating the Madden–Julian oscillation. *J. Climate*, **24**, 2754–2770, doi:[10.1175/2011JCLI3803.1](#).
- , and —, 2014: The moist static energy budget in NCAR CAM5 hindcasts during DYNAMO. *J. Adv. Model. Earth Syst.*, **6**, 420–440, doi:[10.1002/2013MS000272](#).
- Inoue, K., and L. Back, 2015: Column-integrated moist static energy budget analysis on various time scales during TOGA COARE. *J. Atmos. Sci.*, **72**, 1856–1871, doi:[10.1175/JAS-D-14-0249.1](#).
- Jenkins, M. A., and H.-R. Cho, 1991: An observational study of the first-order vorticity dynamics in a tropical easterly wave. *J. Atmos. Sci.*, **48**, 965–975, doi:[10.1175/1520-0469\(1991\)048<0965:AOSOTF>2.0.CO;2](#).
- Johnson, R. H., P. E. Ciesielski, and K. A. Hart, 1996: Tropical inversions near the 0°C level. *J. Atmos. Sci.*, **53**, 1838–1855, doi:[10.1175/1520-0469\(1996\)053<1838:TINTL>2.0.CO;2](#).
- , T. M. Rickenbach, S. A. Rutledge, P. E. Ciesielski, and W. H. Schubert, 1999: Trimodal characteristics of tropical convection. *J. Climate*, **12**, 2397–2418, doi:[10.1175/1520-0442\(1999\)012<2397:TCOTC>2.0.CO;2](#).
- Khouider, B., and A. J. Majda, 2006: A simple multiscalar parameterization for convectively coupled tropical waves. Part I: Linear analysis. *J. Atmos. Sci.*, **63**, 1308–1323, doi:[10.1175/JAS3677.1](#).
- Kikuchi, K., and Y. N. Takayabu, 2004: The development of organized convection associated with the MJO during TOGA COARE IOP: Trimodal characteristics. *Geophys. Res. Lett.*, **31**, L10101, doi:[10.1029/2004GL019601](#).
- Kiladis, G. N., M. C. Wheeler, P. T. Haertel, K. H. Straub, and P. E. Roundy, 2009: Convectively coupled equatorial waves. *Rev. Geophys.*, **47**, RG2003, doi:[10.1029/2008RG000266](#).
- Kim, D., and Coauthors, 2009: Application of MJO simulation diagnostics to climate models. *J. Climate*, **22**, 6413–6436, doi:[10.1175/2009JCLI3063.1](#).
- Kuang, Z., 2008a: Modeling the interaction between cumulus convection and linear gravity waves using a limited-domain

- cloud system-resolving model. *J. Atmos. Sci.*, **65**, 576–591, doi:[10.1175/2007JAS2399.1](https://doi.org/10.1175/2007JAS2399.1).
- , 2008b: A moisture-stratiform instability for convectively coupled waves. *J. Atmos. Sci.*, **65**, 834–854, doi:[10.1175/2007JAS2444.1](https://doi.org/10.1175/2007JAS2444.1).
- , 2011: The wavelength dependence of the gross moist stability and the scale selection in the instability of column-integrated moist static energy. *J. Atmos. Sci.*, **68**, 61–74, doi:[10.1175/2010JAS3591.1](https://doi.org/10.1175/2010JAS3591.1).
- Lin, J.-L., 2007: The double-ITCZ problem in IPCC AR4 coupled GCMs: Ocean–atmosphere feedback analysis. *J. Climate*, **20**, 4497–4525, doi:[10.1175/JCLI4272.1](https://doi.org/10.1175/JCLI4272.1).
- , and Coauthors, 2006: Tropical intraseasonal variability in 14 IPCC AR4 climate models. Part I: Convective signals. *J. Climate*, **19**, 2665–2690, doi:[10.1175/JCLI3735.1](https://doi.org/10.1175/JCLI3735.1).
- Maloney, E. D., 2009: The moist static energy budget of a composite tropical intraseasonal oscillation in a climate model. *J. Climate*, **22**, 711–729, doi:[10.1175/2008JCLI2542.1](https://doi.org/10.1175/2008JCLI2542.1).
- Mapes, B. E., 1997: Equilibrium vs. activation control of large-scale variations of tropical deep convection. *The Physics and Parameterization of Moist Atmospheric Convection*, R. K. Smith, Ed., Springer Netherlands, 321–358, doi:[10.1007/978-94-015-8828-7_13](https://doi.org/10.1007/978-94-015-8828-7_13).
- , 2000: Convective inhibition, subgrid-scale triggering energy, and stratiform instability in a toy tropical wave model. *J. Atmos. Sci.*, **57**, 1515–1535, doi:[10.1175/1520-0469\(2000\)057<1515:CISSTE>2.0.CO;2](https://doi.org/10.1175/1520-0469(2000)057<1515:CISSTE>2.0.CO;2).
- Masunaga, H., and T. S. L'Ecuyer, 2014: A mechanism of tropical convection inferred from observed variability in the moist static energy budget. *J. Atmos. Sci.*, **71**, 3747–3766, doi:[10.1175/JAS-D-14-0015.1](https://doi.org/10.1175/JAS-D-14-0015.1).
- Neelin, J. D., and I. M. Held, 1987: Modeling tropical convergence based on the moist static energy budget. *Mon. Wea. Rev.*, **115**, 3–12, doi:[10.1175/1520-0493\(1987\)115<0003:MTCBOT>2.0.CO;2](https://doi.org/10.1175/1520-0493(1987)115<0003:MTCBOT>2.0.CO;2).
- , and J.-Y. Yu, 1994: Modes of tropical variability under convective adjustment and the Madden–Julian oscillation. Part I: Analytical theory. *J. Atmos. Sci.*, **51**, 1876–1894, doi:[10.1175/1520-0469\(1994\)051<1876:MOTVUC>2.0.CO;2](https://doi.org/10.1175/1520-0469(1994)051<1876:MOTVUC>2.0.CO;2).
- , and N. Zeng, 2000: A quasi-equilibrium tropical circulation model—Formulation. *J. Atmos. Sci.*, **57**, 1741–1766, doi:[10.1175/1520-0469\(2000\)057<1741:AQETCM>2.0.CO;2](https://doi.org/10.1175/1520-0469(2000)057<1741:AQETCM>2.0.CO;2).
- Peters, M. E., and C. S. Bretherton, 2005: A simplified model of the Walker circulation with an interactive ocean mixed layer and cloud–radiative feedbacks. *J. Climate*, **18**, 4216–4234, doi:[10.1175/JCLI3534.1](https://doi.org/10.1175/JCLI3534.1).
- , and —, 2006: Structure of tropical variability from a vertical mode perspective. *Theor. Comput. Fluid Dyn.*, **20**, 501–524, doi:[10.1007/s00162-006-0034-x](https://doi.org/10.1007/s00162-006-0034-x).
- Raymond, D. J., and Ž. Fuchs, 2007: Convectively coupled gravity and moisture modes in a simple atmospheric model. *Tellus*, **59A**, 627–640, doi:[10.1111/j.1600-0870.2007.00268.x](https://doi.org/10.1111/j.1600-0870.2007.00268.x).
- , and —, 2009: Moisture modes and the Madden–Julian oscillation. *J. Climate*, **22**, 3031–3046, doi:[10.1175/2008JCLI2739.1](https://doi.org/10.1175/2008JCLI2739.1).
- , G. B. Raga, C. S. Bretherton, J. Molinari, C. López-Carrillo, and Ž. Fuchs, 2003: Convective forcing in the inter-tropical convergence zone of the eastern Pacific. *J. Atmos. Sci.*, **60**, 2064–2082, doi:[10.1175/1520-0469\(2003\)060<2064:CFITIC>2.0.CO;2](https://doi.org/10.1175/1520-0469(2003)060<2064:CFITIC>2.0.CO;2).
- , S. L. Sessions, and Ž. Fuchs, 2007: A theory for the spinup of tropical depressions. *Quart. J. Roy. Meteor. Soc.*, **133**, 1743–1754, doi:[10.1002/qj.125](https://doi.org/10.1002/qj.125).
- , —, A. H. Sobel, and Ž. Fuchs, 2009: The mechanics of gross moist stability. *J. Adv. Model. Earth Syst.*, **1**, 9, doi:[10.3894/JAMES.2009.1.9](https://doi.org/10.3894/JAMES.2009.1.9).
- , S. Gjorgjievska, S. Sessions, and Ž. Fuchs, 2014: Tropical cyclogenesis and mid-level vorticity. *Aust. Meteor. Ocean J.*, **64**, 11–25.
- Redelsperger, J.-L., F. Guichard, and S. Mondon, 2000: A parameterization of mesoscale enhancement of surface fluxes for large-scale models. *J. Climate*, **13**, 402–421, doi:[10.1175/1520-0442\(2000\)013<0402:APOMEO>2.0.CO;2](https://doi.org/10.1175/1520-0442(2000)013<0402:APOMEO>2.0.CO;2).
- Riley Dellaripa, E. M., and E. D. Maloney, 2015: Analysis of MJO wind-flux feedbacks in the Indian ocean using RAMA observations. *J. Meteor. Soc. Japan*, doi:[10.2151/jmsj.2015-021](https://doi.org/10.2151/jmsj.2015-021), in press.
- Sobel, A. H., 2007: Simple models of ensemble-averaged tropical precipitation and surface wind, given the sea surface temperature. *The Global Circulation of the Atmosphere*, T. Schneider and A. H. Sobel, Eds., Princeton University Press, 219–251.
- , and C. S. Bretherton, 2000: Modeling tropical precipitation in a single column. *J. Climate*, **13**, 4378–4392, doi:[10.1175/1520-0442\(2000\)013<4378:MTPIAS>2.0.CO;2](https://doi.org/10.1175/1520-0442(2000)013<4378:MTPIAS>2.0.CO;2).
- , and —, 2003: Large-scale waves interacting with deep convection in idealized mesoscale model simulations. *Tellus*, **55A**, 45–60, doi:[10.1034/j.1600-0870.2003.201421.x](https://doi.org/10.1034/j.1600-0870.2003.201421.x).
- , and J. D. Neelin, 2006: The boundary layer contribution to intertropical convergence zones in the quasi-equilibrium tropical circulation model framework. *Theor. Comput. Fluid Dyn.*, **20**, 323–350, doi:[10.1007/s00162-006-0033-y](https://doi.org/10.1007/s00162-006-0033-y).
- , and E. Maloney, 2012: An idealized semi-empirical framework for modeling the Madden–Julian oscillation. *J. Atmos. Sci.*, **69**, 1691–1705, doi:[10.1175/JAS-D-11-0118.1](https://doi.org/10.1175/JAS-D-11-0118.1).
- , J. Nilsson, and L. M. Polvani, 2001: The weak temperature gradient approximation and balanced tropical moisture waves. *J. Atmos. Sci.*, **58**, 3650–3665, doi:[10.1175/1520-0469\(2001\)058<3650:TWTGAA>2.0.CO;2](https://doi.org/10.1175/1520-0469(2001)058<3650:TWTGAA>2.0.CO;2).
- , S. Wang, and D. Kim, 2014: Moist static energy budget of the MJO during DYNAMO. *J. Atmos. Sci.*, **71**, 4276–4291, doi:[10.1175/JAS-D-14-0052.1](https://doi.org/10.1175/JAS-D-14-0052.1).
- Straub, K. H., and G. N. Kiladis, 2003: The observed structure of convectively coupled Kelvin waves: Comparison with simple models of coupled wave instability. *J. Atmos. Sci.*, **60**, 1655–1668, doi:[10.1175/1520-0469\(2003\)060<1655:TOSOC>2.0.CO;2](https://doi.org/10.1175/1520-0469(2003)060<1655:TOSOC>2.0.CO;2).
- , P. T. Haertel, and G. N. Kiladis, 2010: An analysis of convectively coupled Kelvin waves in 20 WCRP CMIP3 global coupled climate models. *J. Climate*, **23**, 3031–3056, doi:[10.1175/2009JCLI3422.1](https://doi.org/10.1175/2009JCLI3422.1).
- Su, H., and J. D. Neelin, 2002: Teleconnection mechanisms for tropical Pacific descent anomalies during El Niño. *J. Atmos. Sci.*, **59**, 2694–2712, doi:[10.1175/1520-0469\(2002\)059<2694:TMFTPD>2.0.CO;2](https://doi.org/10.1175/1520-0469(2002)059<2694:TMFTPD>2.0.CO;2).
- Sugiyama, M., 2009: The moisture mode in the quasi-equilibrium tropical circulation model. Part I: Analysis based on the weak temperature gradient approximation. *J. Atmos. Sci.*, **66**, 1507–1523, doi:[10.1175/2008JAS2690.1](https://doi.org/10.1175/2008JAS2690.1).
- Tian, B., and V. Ramanathan, 2003: A simple moist tropical atmosphere model: The role of cloud radiative forcing. *J. Climate*, **16**, 2086–2092, doi:[10.1175/1520-0442\(2003\)016<2086:ASMTAM>2.0.CO;2](https://doi.org/10.1175/1520-0442(2003)016<2086:ASMTAM>2.0.CO;2).
- Webster, P. J., and R. Lukas, 1992: TOGA COARE: The Coupled Ocean–Atmosphere Response Experiment. *Bull. Amer. Meteor. Soc.*, **73**, 1377–1416, doi:[10.1175/1520-0477\(1992\)073<1377:TCTCOR>2.0.CO;2](https://doi.org/10.1175/1520-0477(1992)073<1377:TCTCOR>2.0.CO;2).
- Yanai, M., S. Esbensen, and J.-H. Chu, 1973: Determination of bulk properties of tropical cloud clusters from large-scale heat

- and moisture budgets. *J. Atmos. Sci.*, **30**, 611–627, doi:[10.1175/1520-0469\(1973\)030<0611:DOBPOT>2.0.CO;2](https://doi.org/10.1175/1520-0469(1973)030<0611:DOBPOT>2.0.CO;2).
- Yu, J.-Y., and J. D. Neelin, 1994: Modes of tropical variability under convective adjustment and the Madden–Julian oscillation. Part II: Numerical results. *J. Atmos. Sci.*, **51**, 1895–1914, doi:[10.1175/1520-0469\(1994\)051<1895:MOTVUC>2.0.CO;2](https://doi.org/10.1175/1520-0469(1994)051<1895:MOTVUC>2.0.CO;2).
- , C. Chou, and J. D. Neelin, 1998: Estimating the gross moist stability of the tropical atmosphere. *J. Atmos. Sci.*, **55**, 1354–1372, doi:[10.1175/1520-0469\(1998\)055<1354:ETGMSO>2.0.CO;2](https://doi.org/10.1175/1520-0469(1998)055<1354:ETGMSO>2.0.CO;2).
- Zebiak, S. E., 1986: Atmospheric convergence feedback in a simple model for El Niño. *Mon. Wea. Rev.*, **114**, 1263–1271, doi:[10.1175/1520-0493\(1986\)114<1263:ACFIAS>2.0.CO;2](https://doi.org/10.1175/1520-0493(1986)114<1263:ACFIAS>2.0.CO;2).
- Zhang, M. H., and J. L. Lin, 1997: Constrained variational analysis of sounding data based on column-integrated budgets of mass, heat, moisture, and momentum: Approach and application to ARM measurements. *J. Atmos. Sci.*, **54**, 1503–1524, doi:[10.1175/1520-0469\(1997\)054<1503:CVAOSD>2.0.CO;2](https://doi.org/10.1175/1520-0469(1997)054<1503:CVAOSD>2.0.CO;2).